

# Evaluation of the coupled effect of strain localization and asymmetric damage distribution on rope response: Numerical approach based on a nonlinear cable-beam element

Juan Felipe Beltrán<sup>a,\*</sup>, Tomás Bravo<sup>b</sup>

<sup>a</sup> Dept. of Civil Engineering, University of Chile, Blanco Encalada # 2002 Of. 440, Santiago, Chile

<sup>b</sup> Dept. of Civil Engineering, University of Chile, Blanco Encalada # 2002, Santiago, Chile

## ARTICLE INFO

### Keywords:

Damage  
Finite element method  
Numerical simulation  
Rope failure  
Rope response  
Nonlinear cable-beam element

## ABSTRACT

In this paper, a numerical model to evaluate the impact of the presence of fractured rope components on the static response of ropes is presented. Specifically, the proposed model couples the effects of two phenomena that rule damaged rope response: strain localization and asymmetry in damage distribution. The proposed model relies on the nonlinear finite element method in which the damaged rope is discretized along its length into 3D uniaxial two-noded nonlinear cable-beam elements with Bernoulli's kinematic hypothesis. These elements account for the helical structure of a rope (cable) as well as the axial-bending, axial-torsional, and bending-torsional interactions. Experimental static tensile test data reported in the literature of homogeneous polyester ropes with overall diameters that range from 32 mm to 166 mm are used to validate the proposed model. Tested ropes are asymmetrically damaged on the surface of the rope cross-sections in which initial damage levels (percentage of the broken components of the damaged cross-section with respect to the intact rope) vary from 5% to 15%. Comparison results indicate that the proposed model accurately predicts the static response of damaged ropes, considering a wide range of rope diameter and damage level values, achieving numerical robustness and computational efficiency.

## 1. Introduction

Ropes are characterized by having a high axial strength and stiffness in relation to their weight, combined with a low flexural stiffness. This combination is achieved by using a large number of components, each of which is continuous throughout a rope's length. To facilitate handling, it is necessary to ensure that a rope has some integrity as a structure, rather than being merely a set of parallel components. This characteristic is achieved by twisting the components together [1].

Over the years, ropes made from filaments drawn from ductile metals and synthetic polymers have been widely used as structural members in various engineering industries. Such uses include ropes for lifting materials and equipment at construction sites, mooring systems, electrical conductors, mine hoisting, stayed bridges, anticollision and protective nets, cranes, and so on [2,3].

Ropes (cables) experience damage throughout their loading history and from continued aggression of the environment (urban, industrial, marine, etc.). Damage to ropes degrades rope components properties, a process that may induce the partial or complete rupture of some of

them, and eventually, compromise the safety and integrity of the structural system that the damaged ropes are part of. Hence, the understanding of the interaction of the factors that induce damage to ropes, their dependence on the rope operational conditions, and the effects of damage on the mechanical behavior of ropes are essential to estimate rope service life at the design stage and to establish the appropriate rope inspection methods and discard criteria [4–6].

The studies previously conducted, mainly on steel wire and synthetic fiber ropes, have shown that the impact of broken rope components on overall rope response (stiffness, residual strength, deformation capacity, and deformed configuration) depends on the length of the rope, number of broken rope components (degree of damage or damage level), type of rope construction, and their distributions throughout the rope cross-section (symmetric and asymmetric) and along the rope length. These studies have intended experimentally ([7–13] among others) and numerically ([13–23]) to assess the ability of particular types of rope constructions to withstand damage (i.e., damage-tolerance property), according to rope application.

In particular, Beltrán et al. [23] studied the effects of two

\* Corresponding author.

E-mail addresses: [jbeltran@ing.uchile.cl](mailto:jbeltran@ing.uchile.cl) (J.F. Beltrán), [tomas.bravo@ing.uchile.cl](mailto:tomas.bravo@ing.uchile.cl) (T. Bravo).

mechanisms that govern the behavior of damaged ropes: strain localization around the failure region ([19]) and asymmetric damage distribution at a given rope cross-section ([21]). A semi-analytical proof was given to show that, acting independently, strain localization and asymmetry in damage distribution phenomena provide upper and lower bounds, respectively, to the response of damaged ropes. In this study, the experimental data reported in [10] on large-scale damaged polyester ropes (diameters vary from 32 mm to 166 mm) were interpreted, concluding that strain localization and asymmetric damage distribution mechanisms rule the static response of the tested ropes in terms of the rope stiffness and reductions in strength and deformation capacity relative to the virgin case.

In this paper, to the best knowledge of the authors, a first attempt to study the coupled effects of strain localization and asymmetry in damage distribution on the static response of damaged ropes using a robust and computational efficient numerical model is presented. The proposed model relies on the finite element method in which the damaged rope is discretized along its length into 1D two-noded nonlinear cable-beam elements with six degrees of freedom (dof) per node and Bernoulli's kinematic hypothesis. These elements account for the helical structure of a rope (cable) as well as the axial-bending, axial-torsional, and bending-torsional interactions. The analysis conducted on experimental static tensile tests data reported in [10] presented in [23] is revised for validation purposes and also to interpret them based on the simulations provided by the proposed model.

## 2. Cable-beam element formulation

As previously stated, previous researches ([8,10,13,16,21]) have shown that two of the main mechanisms that govern the response of damaged ropes are strain localization and asymmetry in damage distribution, in which bending deformation takes place in ropes due to the latter mechanism; thus, ropes eventually undergo changes in curvature. Under this condition, a flexible model (rope treated as a fiber element, i.e., slender body of negligible bending and torsional stiffness) is inadequate to accurately describe the mechanical behavior of the damaged rope. In this kind of problem, a richer model for the rope should be developed in which axial, torsion, and bending strains as well as axial-bending, axial-torsion, and bending-torsion interactions need to be accounted for (the so-called stiff cable model) ([24,25]).

In previous works, the stiff cable-based model has been adopted with different degrees of complexity to study rope (or power line conductor) response under different types of loading conditions such as remotely operated vehicle systems, transverse vibrations, and bending loads ([21,26–32] among others). In the particular case of the study of damaged ropes, to capture the coupled effects of the strain localization and asymmetry in damage distribution phenomena, the rope is assumed to behave as a stiff rope which means that it can be subjected to biaxial bending and axial load and moment. As such, based on the standard finite element procedure, it is proposed to discretize the rope into 1D two-noded nonlinear cable-beam (stiff cable) elements with six degree of freedom per node and Bernoulli's kinematic hypothesis that account for the helical structure of a rope (cable) as well as the axial-bending, axial-torsional, and bending-torsional interactions. The latter hypothesis is coherent with previous works ([13,21,29,31,32]) and with the facts that the rope is assumed to be a slender element, limited lateral deflections and rope cross-section deformation are presumed, and the results provided with satisfactory accuracy by a numerical algorithm based on the Euler-Bernoulli beam theory in assessing the strain field of metallic strands asymmetrically damaged on their surfaces ([13]). In the following, a description of the formulation of the proposed cable-beam element is presented.

### 2.1. Incremental virtual work equation

It is first provided a concise summary of the traditional and well

accepted procedure for the nonlinear analysis of structures based on the principle of virtual work (i.e., nonlinear finite element method), considering the updated Lagrangian formulation. Assuming that rope components mainly behave as thin curved fiber elements (i.e., they only develop uniaxial state of stress), an incremental form of the constitutive law of the material that comprises them can be written in the following form:

$$\Delta\sigma_j = (E_t)_{j-1}\Delta\varepsilon_j \quad (1)$$

where  $\Delta\sigma_j$  and  $\Delta\varepsilon_j$  are the increments in the normal stress and axial strain for the  $j$ -th step of the analysis; and  $(E_t)_{j-1}$  is the tangent modulus at the  $(j-1)$  step of the analysis. Considering that the increment in the axial strain  $\Delta\varepsilon_j$  can be decomposed in its linear ( $\Delta\varepsilon_j$ ) and nonlinear ( $\Delta\eta_j$ ) terms of the updated Green strain increment tensor for the  $j$ -th step of the analysis ([33]) and the fact that the  $j$ -th step of the analysis is an equilibrium configuration, the linearized version of the increment in the internal virtual work for a generic rope element is given by

$$(\delta W_{int})_j = \int_{V_{j-1}} (E_t)_{j-1}\Delta\varepsilon_j\delta_{j-1}edV_{j-1} + \int_{V_{j-1}} \sigma_{j-1}\delta_{j-1}edV_{j-1} + \int_{V_{j-1}} \sigma_{j-1}\delta_{j-1}\eta_dV_{j-1} \quad (2)$$

where  $V_{j-1}$  is the volume of the element over which energy is computed in the  $j-1$  step of the analysis and the operator  $\delta_{j-1}$  refers to a virtual variation of the variable operated upon based on the  $(j-1)$  configuration. The usual tensor notation has been simplified considering that rope components are assumed to behave mainly as fiber elements,  $\sigma = \sigma_{tt}$ ,  $\varepsilon = \varepsilon_{tt}$ ,  $e = e_{tt}$ , and  $\eta = \eta_{tt}$  in which  $t$  corresponds to the longitudinal local axis of the rope component.

Applying the principle of virtual works yields

$$\int_{V_{j-1}} (E_t)_{j-1}\Delta\varepsilon_j\delta_{j-1}edV_{j-1} + \int_{V_{j-1}} \sigma_{j-1}\delta_{j-1}\eta_dV_{j-1} = \int_{V_{j-1}} (f_k)_j\delta u_k dV_{j-1} + \int_{A_{j-1}} (t_k)_j\delta u_k dA_{j-1} - \int_{V_{j-1}} \sigma_{j-1}\delta_{j-1}edV_{j-1} \quad (3)$$

where the first two terms of the right-hand side of the above equation correspond to the increment in the external virtual work ( $\delta W_{ext}$ ) in the  $j$ -th step of the analysis. In the latter,  $(f_k)_j$  and  $(t_k)_j$  are the  $k$ th components of the body and surface forces, respectively in the  $j$  step of the analysis;  $A_{j-1}$  is the surface element in the  $j-1$  step of the analysis, and  $u_k$  is the  $k$ th component of the displacement field.

Following the notation proposed in [33], the terms of the right hand side of Eq. (3), can be grouped in the following manner:

$$F_{j-1}^j = \int_{V_{j-1}} (f_k)_j\delta u_k dV_{j-1} + \int_{A_{j-1}} (t_k)_j\delta u_k dA_{j-1} \quad (4a)$$

$$F_{j-1}^{j-1} = \int_{V_{j-1}} \sigma_{j-1}\delta_{j-1}edV_{j-1} \quad (4b)$$

As such, the Eq. (3) can be recast as follows:

$$\int_{V_{j-1}} (E_t)_{j-1}\Delta\varepsilon_j\delta_{j-1}edV_{j-1} + \int_{V_{j-1}} \sigma_{j-1}\delta_{j-1}\eta_dV_{j-1} = F_{j-1}^j - F_{j-1}^{j-1} \quad (4c)$$

### 2.2. Kinematic of a cable-beam element in a 3D- space

Consider a straight prismatic two-noded cable-beam element of length  $L$  depicted in Fig. 1. The element has a total of twelve degrees of freedom (dofs), in which  $x$  denotes the longitudinal axis and  $(y, z)$  the two principal axes of the cross-section. The displacements of a standard two-noded cable-beam element in a 3D-space consist of three translation  $u$ ,  $v$ , and  $w$  in  $x$ ,  $y$ , and  $z$  directions, and three rotations  $\theta_x$ ,  $\theta_y$ , and  $\theta_z$ , around axes  $x$ ,  $y$ , and  $z$  respectively, which are functions of the position  $x$  along the element. For the generic element  $b$  with length  $L_b$  depicted in Fig. 1, nodal displacements are collected in the displacement vector  $\{u\}_b$ :

$$\{u\}_b = [u_1 v_1 w_1 \theta_{x1} \theta_{y1} \theta_{z1} u_2 v_2 w_2 \theta_{x2} \theta_{y2} \theta_{z2}]_b^T \quad (5)$$

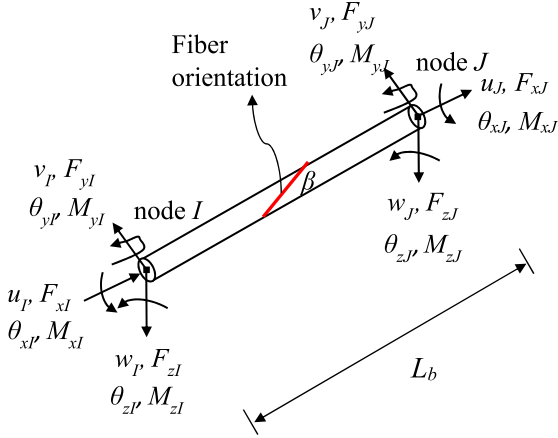


Fig. 1. Generic two-noded stiff cable-beam element  $b$  in a 3D-space.

### 2.3. Section kinematics

Previously stated, it is assumed that the generic cable-beam element obeys the Euler-Bernoulli's kinematic hypothesis. As such, the displacements  $\{u^m\}(x,y,z)$  of a material point  $m$  with coordinates  $(y,z)$  at a section with distance  $x$  from the origin of the reference frame, that describe the rigid body motion of the section plane, are given by the following expressions:

$$u_t^m(x, y, z) = (u(x) - y\theta_z(x) + z\theta_y(x))\cos\beta^m + \sqrt{z^2 + y^2}\theta_x(x)\sin\beta^m \quad (6a)$$

$$u_y^m(x, y, z) = v(x) - z\theta_x(x) \quad (6b)$$

$$u_z^m(x, y, z) = w(x) + y\theta_x(x) \quad (6c)$$

where  $u_t^m$  corresponds to the displacement in the  $t$  direction of the material point  $m$  that is part of a fiber oriented in an angle  $\beta$  relative to the  $x$  axis. In this way, the orientation of the rope components, that in their initial configurations correspond to a circular helix curve, are accounted for (Fig. 1). The transverse displacements  $u_y^m$  and  $u_z^m$  of the material point  $m$  are assumed to be small based on previous works on asymmetrically damaged ropes ([13,21]); thus, the same transverse displacements of a fiber aligned along the longitudinal axis of the rope are considered for the case of a fiber inclined relative to the latter due to its initial helical geometry along with neglecting their contributions to  $u_t^m$ . In the above expressions, it is important to point out that the following kinematic relations hold:  $\theta_z(x) = dv(x)/dx$  and  $\theta_y(x) = dw(x)/dx$ , where  $d(\cdot)/dx$  is the first derivative operator acting on the corresponding function.

Considering that rope components are assumed to behave as fiber elements; the only term of the updated Green strain increment tensor accounted for the computation internal virtual work in Eq. (2) is given by

$$\varepsilon_{tt}^m = \frac{\partial u_t^m}{\partial t} + \frac{1}{2} \left[ \left( \frac{\partial u_t^m}{\partial t} \right)^2 + \left( \frac{\partial u_y^m}{\partial t} \right)^2 + \left( \frac{\partial u_z^m}{\partial t} \right)^2 \right] \quad (7)$$

where the first and second term correspond to the linear ( $e_{tt}^m$ ) and nonlinear ( $\eta_{tt}^m$ ) terms of  $\varepsilon_{tt}^m$ .

It is important to point out that the displacement and rotation functions  $u(x)$  and  $\theta_p(x)$  ( $p = x, y,$  and  $z$ ) respectively, depend on the variable  $x$  (longitudinal axis of the rope); thus, computation of the derivatives with respect to  $t$  (local longitudinal axis of the rope components) in the above equation, gives rise to the terms  $\cos\beta$ ,  $\cos^2\beta$ ,  $\cos^3\beta$ ,  $\cos^2\beta\sin\beta$ , and  $\sin\beta\cos\beta$  in the expression for  $\varepsilon_{tt}^m$  due to the helical nature of the rope components. Therefore, the expression for  $\varepsilon_{tt}^m$  in terms of the derivatives with respect to  $x$  is given by

$$\varepsilon_{tt}^m = \frac{\partial u_t^m}{\partial x} \cos\beta^m + \frac{1}{2} \left[ \left( \frac{\partial u_t^m}{\partial x} \right)^2 + \left( \frac{\partial u_y^m}{\partial x} \right)^2 + \left( \frac{\partial u_z^m}{\partial x} \right)^2 \right] (\cos\beta^m)^2 \quad (8)$$

where  $u_t^m$ ,  $u_y^m$ , and  $u_z^m$  are given by Eqs. (6a–c).

### 2.4. Cable-beam stiffness matrix

By utilizing a standard finite element procedure, the virtual work equation (Eq. (4c)), applied to a generic cable-beam element  $b$  that is part of the rope discretization, can be turned into an incremental algebraic equation for the generic element from the step of the analysis  $j-1$  to  $j$  as

$$([k_L] + [k_G])_{j-1,b}^{j-1} \{du\}_{j-1,b}^j = (f_{j-1}^j - f_{j-1}^{j-1})_b \quad (9)$$

where  $[k_L]_b$  and  $[k_G]_b$  are the local linear and geometric stiffness matrices of element  $b$ , respectively;  $\{du\}_b$  increment in nodal displacement vector of element  $b$ ; and  $(f_{j-1}^j - f_{j-1}^{j-1})_b$  is the increment in nodal forces vector from the step of the analysis  $j-1$  to  $j$  of element  $b$ , in which both quantities are referred to the deformed configuration of the element  $b$  related to  $j-1$  step of the analysis. Expressions to derive the aforementioned stiffness matrices and nodal load vector are provided in Appendix A.

The interpolation functions selected for the trial kinematic variables functions  $v(x)$ ,  $w(x)$ ,  $\theta_z(x)$ , and  $\theta_y(x)$  and their corresponding virtual forms correspond to the well-known Hermite cubic polynomials and for the case of  $u(x)$  and  $\theta_x(x)$  linear interpolations functions are used for trial and virtual ones (Appendix A). In addition, increments in trial and virtual strains necessary to compute  $[k_L]_b$  and  $[k_G]_b$  according to Eqs. (A.1) and (A.2) respectively, are obtained by applying the variation ( $\Delta$ ) and virtual ( $\delta$ ) operators to Eq. (8) in the traditional way used in finite element procedure ([33–35] among others). In Appendix B, the explicit forms of  $[k_L]_b$  and  $[k_G]_b$  for a generic cable-beam element  $b$  are provided.

### 2.5. Nodal forces. Surface damage asymmetrically distributed case.

In this study, a particular type of polyester rope construction is considered for illustrative purposes. Rope geometry analyzed consists of a group of parallel sub-ropes in which each sub-rope is built by twisting three strands together with diameters that vary from 32 mm to 166 mm. Rope is covered by a protective braided jacket with specified undamaged breaking strength (SBS) rope values equal to 35 tonnes (343.2 kN) and 700 tonnes (6864.6 kN) and the initial surface damage level values of rope cross-sections range from 5% to 15% ([10]).

Considering that damaged ropes are discretized into several cable-beam elements, based on [21], it is proposed that each cable-beam element  $b$  have a prismatic section and be subjected to biaxial sinusoidal type of loadings  $(q_z, q_y)_b$  acting along its principal directions. The latter loads account for the fact that the symmetry of the rope cross-section is lost due to asymmetric damage distribution which is giving rise to a net transverse force per unit length of rope  $q_{R,b}$  in which broken strands are colored black (Fig. 2a). More details on the computation of  $q_z$  and  $q_y$  values (Fig. 2b) are provided in the subsequent paragraphs. Nodal forces  $\{P\}_b$ , and  $\{Q\}_b$  associated to  $(q_z, q_y)_b$  respectively, are computed based on the interpolations functions used to approximate  $v(x)$ ,  $w(x)$ ,  $\theta_z(x)$ , and  $\theta_y(x)$  (Fig. 1), which is this case correspond to the Hermite cubic polynomials functions, that are defined in Appendix A ([33–35]). The corresponding nodal forces are depicted in Fig. 1 with their corresponding dof.

The procedure to assess  $(q_z, q_y)_b$  values, for the particular ropes constructions analyzed in this study, first considers the analysis of the damaged strands in which the local (relative to reference systems associated to each strand) radial unbalanced forces  $q_1$  and  $q_2$  are computed which are then added vectorially to find the net unbalanced line force acting on the cross-section  $q_{R,b}$  (Fig. 2a). Complete details of this

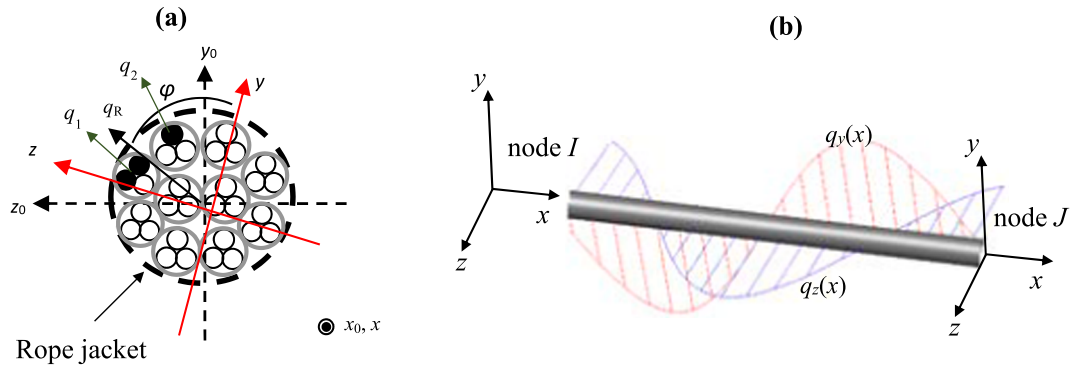


Fig. 2. (a) Asymmetrically damaged rope cross-section; (b) nonlinear generic cable-beam element under sinusoidal loads.

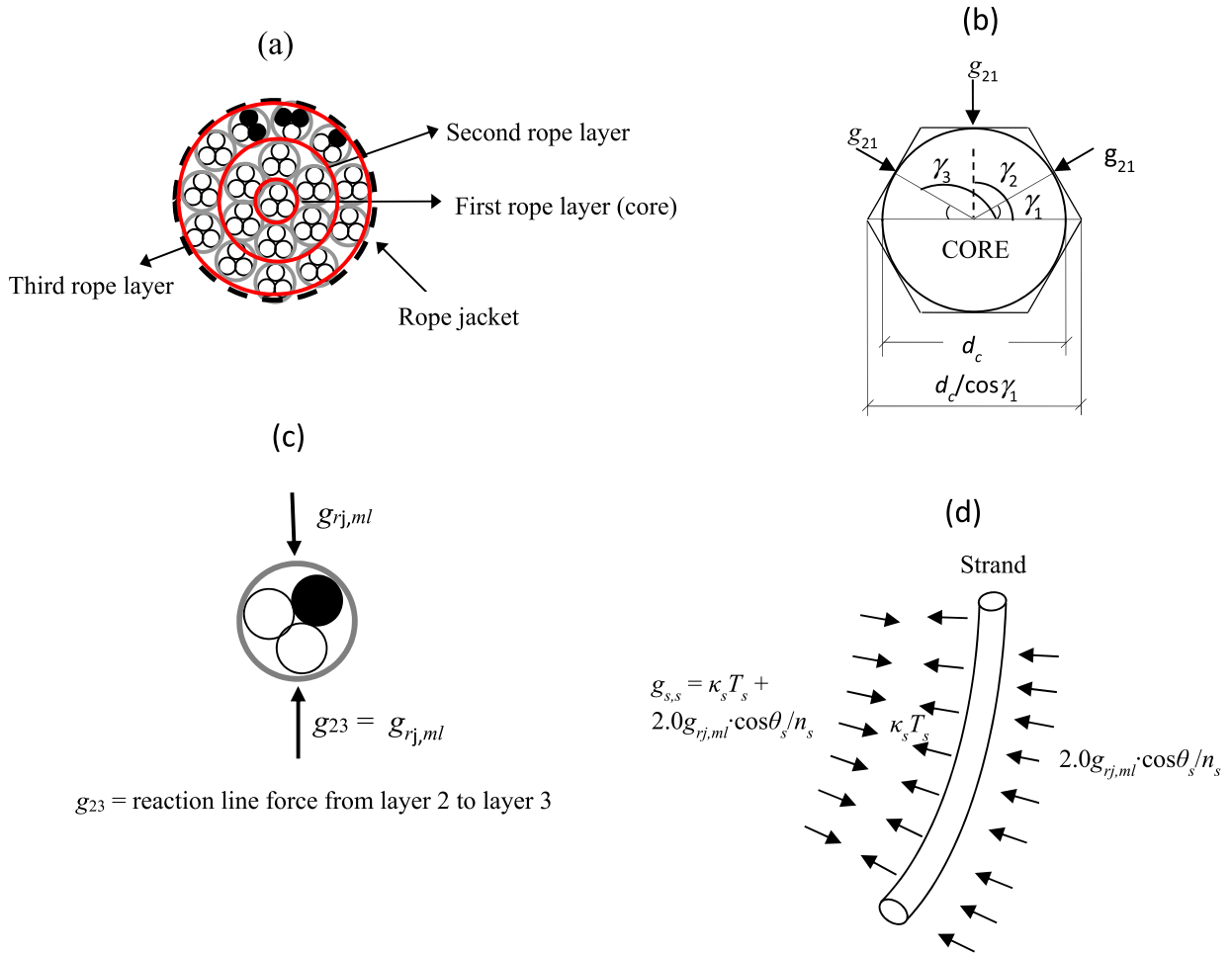


Fig. 3. (a) Damaged rope cross-section; (b) compressive line forces acting on the rope core; (c) normal forces on subrope; (d) strand equilibrium.

procedure is provided in [23]. The line force  $q_{R,b}$  forms an angle  $\varphi$  relative to an arbitrary axis  $y$ . Due to the helical nature of the strands, this axis coincides with one of the principal axes of the damaged rope cross-section for increasing values of  $\varphi$  (Fig. 2a) equal to  $n\pi/2$  ( $n$  is an integer). Considering a damaged cross-section in which the arbitrary  $xy$  and  $xz$  planes coincide with principal ones (Fig. 2a), the net transverse line forces along the longitudinal axis of the ropes in both the  $xz$  and  $xy$  (principal) planes are given by

$$q_{z,b} = q_{R,b} \sin \varphi \tag{10a}$$

$$q_{y,b} = q_{R,b} \cos \varphi \tag{10b}$$

in which the angle  $\varphi$  captures the dependence of the line force  $q_R$  on

the helical nature of strands in the initial rope configuration. The angle  $\varphi$  varies according to the following relationship:  $\varphi = (2\pi x / p_s)$ , where  $p_s$  is the pitch distance of the strands relative to the local longitudinal axis of damaged subropes as described in [23].

### 3. Damaged rope discretization

The finite element model proposed to study damaged rope response, relies on the ability of broken rope components to carry their proportionate share of axial loads over a distance measured from the failure region, which is referred as the *recovery length* ( $rl$ ) ([36]). Along this length, the model accounts for the potential continuous increment of the contribution to damaged rope response of the broken components

along with the fact that the asymmetry of the rope cross-section is diminished. As long as the broken rope components do not fully develop their recovery length values, the formulation of the proposed model accounts for the strain localization and asymmetry in damage distribution, as well as their interaction effects on rope response.

Rope discretization depends on the recovery length values estimated, because in this region the coupling between strain localization and asymmetry in damage distribution occurs, inducing a premature failure of the ropes relative to the virgin case according to previous works ([10,23,37]). Recovery lengths values depend on the frictional forces developed in a rope, contact forces between rope components (due to their helical nature and/or jacket confinement) and the surface characteristics (i.e., friction coefficient) of the components in contact ([37]). For the particular type of rope construction considered in this study (helical strands assembled parallel to each other) and from the numerical simulation point of view, strain localization around the failure region is primarily developed by rope jacket confinement ([10,19,23]), neglecting the potential contribution of the helical strands construction; thus, in terms of the finite element modeling, the effect of rope jacket confinement on the recovery length value must be assessed.

### 3.1. Estimate of recovery length values

Consider the damaged rope cross-section depicted in Fig. 3a, in which broken rope components (strands) are colored black. This rope is formed by 18 parallel subropes arranged in three layers (red circles in Fig. 3a) confined by a polyester jacket (dashed black circle in Fig. 3a). Likewise, subropes are formed by three-strands twisted together along a fictitious local longitudinal axis. According to the results given in [37], if the value of the tension in a broken strand ( $T_s$ ) is prescribed for a particular rope strain value, the recovery length value ( $rl$ ) of a broken strand, considering a Coulomb friction model, can be estimated as

$$rl = \frac{1}{\mu C_2} \ln \left[ \frac{\mu C_2 T_s}{C_1} + 1 \right] \quad (11)$$

where  $\mu$  is the friction coefficient,  $C_1$  value is the normal force per unit length acting on the broken strand independent of the  $T_s$  value; and  $C_2$  is a constant associated to the normal force acting on the broken strand that depends on the  $T_s$  due to its helical nature.

Assuming deformation compatibility between rope jacket and subropes and that the rope jacket develops longitudinal and circumferential stresses according to the assumptions of thin-walled tube behavior, the compression forces,  $g_{rj,ml}$ , exerted by the rope jacket ( $rj$ ) on the rope components of the outermost layer ( $ml$ ) of a rope (Fig. 3a) can be estimated as ([19])

$$g_{rj,ml} = \frac{2n_2}{dn_{ml} \sum_{i=1}^3 \sin \gamma_i} \left( \frac{d_c}{\cos \gamma_i} \right) (2\sigma_L t) \quad (12)$$

where  $d$  is the rope diameter;  $n_2$ ,  $n_{ml}$  are the number of rope components in the second and outermost layer (third layer in this example) of the rope;  $d_c$  is the core diameter (subrope in the first layer); and the angle  $\gamma_i$  is defined in Fig. 3b. In the latter, symmetry condition related to the contact line forces  $g_{21}$  exerted by the subropes of the second layer on the rope core is used in which three out of six line forces are depicted. The value of  $\sigma_L$  is the longitudinal stress in the rope and  $t$  is the thickness of the rope jacket. Thus, assuming mainly radial contact between subropes, the total normal line force  $N_{ml}$  exerted on a rope component of the outermost layer of the rope that has a broken strand is given by  $N_{ml} = 2.0g_{rj,ml}$  (Fig. 3c). In this way, assuming continuous transmission of the  $N_{ml}$  line force to the strands (Fig. 3d), the total normal line force on the broken strand  $N_s$  is assessed as

$$N_s = \frac{4.0g_{rj,ml}}{n_s} \cos \beta_s + \kappa_s T_s \quad (13)$$

where  $n_s$  is the number of the strand that form the subrope and  $\beta_s$  is the

helix angle of the strands. In Fig. 3d,  $g_{s,s}$  is the reaction line force exerted on each strand by the others two strand and  $\kappa_s T_s$  is the radial line body force necessary to preserve the helical geometry of the strand ([38]). By radial equilibrium,  $g_{s,s} = \kappa_s T_s + 2.0g_{rj,ml} \cos \theta_s / n_s$ . Hence, based on the explanations of Eqs. (11) and (12), it is drawn that

$$C_1 = \frac{4.0g_{rj,ml}}{n_s} \cos \beta_s; C_2 = \kappa_s \quad (14)$$

Values of the recovery length of the broken strands for the ropes analyzed in this study obtained from Eq. (11), are provided in Section 4 Numerical simulations and discussion.

### 3.2. Numerical algorithm procedure

A standard nonlinear finite element procedure ([33,35,39] among others) is implemented to assess static damaged ropes responses. In a general case, damaged rope discretization strongly relies on the  $rl$  value of the rope due to the nonuniform axial strain distribution along this length which results in an axial strain localization around the fracture zone. This nonlinear finite element procedure is based on an iterative displacement control algorithm for each increment of the rope axial displacement. The incremental-iterative equation of global equilibrium in a nonlinear finite element procedure has the following form:

$$[(K_L)_{dr} + (K_G)_{dr}]_{j-1}^{k-1} \{d\mathbf{u}\}_j^k = \{d\mathbf{Q}\}_j^k + \{\mathbf{R}\}_j^{k-1} \quad (15)$$

where  $[(K_L)_{dr}]$  and  $[(K_G)_{dr}]$  are the linear and geometric stiffness matrices respectively whose addition is equal to  $[K_{dr}]$  which is the tangent stiffness matrix of the damaged rope;  $\{d\mathbf{u}\}$  and  $\{d\mathbf{Q}\}$  are the increment in the displacement and in the external load vectors respectively;  $\{\mathbf{R}\}$  is the residual load vector (difference between internal and external loads); and subscript  $j$  and superscript  $k$  represent the step of the analysis and the number of iterations in that step respectively. The entities  $[K_{dr}]$ ,  $\{d\mathbf{Q}\}$ , and  $\{\mathbf{R}\}$  are referenced to a fixed global coordinate system and they are obtained utilizing standard assembly procedures for the damaged rope stiffness and load vectors, in which the local stiffness matrix  $[k]_b = [k_L]_b + [k_G]_b$  and nodal forces vectors  $\{P\}_b$  and  $\{Q\}_b$  for each cable-beam element  $b$  are determined in global coordinate system through the use of transformation matrices as discussed in Appendix C. In the above discussion, bold variables refers to (vectors) entities associated to the global response of the damaged rope analyzed.

In particular, the entity  $[K_{dr}]$  is computed by accounting for the partial contribution of initially broken strands according to the location of each cable-beam element  $b$  relative to the recovery length ( $rl$ ) value given by Eq. (11), as illustrated in Appendix B. The proposed algorithm proceeds with the following steps for the  $j$ th incremental step of the analysis:

**Step 1:** Prescribe an increment in axial rope displacement  $du_j$ . Based on Eq. (15), solve the following system of equations considering the superscript (iterations)  $k$  equal to 1:

$$[K_{dr}]_{j-1}^0 \{d\mathbf{u}\}_j^1 = \{d\mathbf{Q}\}_j^1 \quad (16)$$

The prescribed value of  $du_j$  induces an increment in the axial load of the rope  $dT_j^1$  which can be estimated as

$$dT_j^1 = \sum_{\substack{\text{unbroken} \\ \text{strands}}} A_s (E_s)_{j-1} (\cos \beta_s)_{j-1}^3 \frac{du_j}{L_{j-1}} \quad (17)$$

where  $A_s$  is the cross-sectional area of the strands;  $(E_s)_{j-1}$  and  $(\beta_s)_{j-1}$  are the tangent modulus and helix angle of the unbroken strands at the end of the  $(j-1)$ th increment of the analysis; and  $L_{j-1}$  is the updated rope length at the end of the  $(j-1)$ th increment of the analysis. The value of  $\{d\mathbf{Q}\}_j^1$  is estimated based on the  $dT_j^1$  value and on the incremental form of the expressions for nodal load vectors  $\{P\}_b$ , and  $\{Q\}_b$ , in which the values of  $(dq_{y,b})_j^1$  and  $(dq_{z,b})_j^1$  are computed as follows:

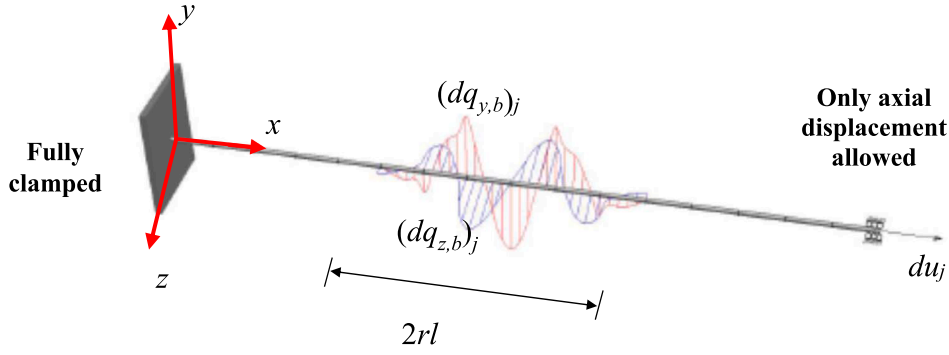


Fig. 4. Damaged rope discretized into two-noded stiff cable-beam elements.

$$(dq_{y,b})_j^1 = \left[ (\kappa_s)_{j-1} A_s (E_s)_{j-1} (\cos \beta_s)_{j-1} \frac{du_j}{L_{j-1}} \sqrt{G_1^2 + G_2^2 - 2G_1 G_2 \cos \alpha} \right]_b \cos \varphi \quad (18a)$$

$$(dq_{z,b})_j^1 = \left[ (\kappa_s)_{j-1} A_s (E_s)_{j-1} (\cos \beta_s)_{j-1} \frac{du_j}{L_{j-1}} \sqrt{G_1^2 + G_2^2 - 2G_1 G_2 \cos \alpha} \right]_b \sin \varphi \quad (18b)$$

where the above expressions for each cable-beam element  $b$  depend on their positions along the rope according to its finite element discretization (captured by the angle  $\varphi$ ) and the degree of contribution to rope response of the broken strands based upon the  $rl$  value computed using Eq. (11) (Fig. 4). The latter is captured by the constants  $G_i$  in Eqs. (18a) and (b) that account for the damage level of initially broken strands ( $D_s$ ) in each cable-beam element  $b$  as explained in Appendix C. These expressions are estimated based on the work [23] for the specific damaged section depicted in Fig. 2a. Thus, the increment and total values of the nodal forces are as follows:

$$\{dQ\}_{b,j}^1 = \int_{L_b} [N_{\partial z}]^T (dq_{y,b})_j^1 d\xi \quad (19a)$$

$$\{dP\}_{b,j}^1 = \int_{L_b} [N_{\partial y}]^T (dq_{z,b})_j^1 d\xi \quad (19b)$$

$$\{Q\}_{b,j}^1 = \{Q\}_{b,j-1} + \{dQ\}_{b,j}^1 \quad (20a)$$

$$\{P\}_{b,j}^1 = \{P\}_{b,j-1} + \{dP\}_{b,j}^1 \quad (20b)$$

where  $[N_{\partial z}]$  and  $[N_{\partial y}]$  are defined in Appendix A. The parameters  $\alpha$  and  $\psi_s$  are the angles between  $q_1$  and  $q_2$  and between the contact line force direction of unbroken strand which points to the centroid of the equilateral triangle that forms the three-strand configuration (subrope with one broken strand; Fig. 2a), relative to the base of this equilateral triangle (i.e.,  $30^\circ$  in this example) respectively.

For solution purposes, Eq. (16) can be recast in the following form:

$$\begin{bmatrix} [K_{ff}] & [K_{fc}] \\ [K_{cf}] & [K_{cc}] \end{bmatrix}_{j-1}^0 \begin{Bmatrix} \{du_f\}_j^1 \\ \{du_c\}_j^1 \end{Bmatrix} = \begin{Bmatrix} \{dB_f\}_j^1 \\ \{dB_c\}_j^1 \end{Bmatrix} + \begin{Bmatrix} \{dF_f\}_j^1 \\ \{dF_c\}_j^1 \end{Bmatrix} \quad (21)$$

where the subscripts  $f$  and  $c$  refer to unknown and known variables respectively; and  $B$  and  $F$  are the reactions and equivalent nodal loads vectors respectively. The solution of the above system of equation gives

$$\{du_f\}_j^1 = [[K_{ff}]_{j-1}^0]^{-1} \{ \{dF_f\}_j^1 - [K_{fc}]_{j-1}^0 \{du_c\}_j^1 \} \quad (22a)$$

$$\{dB_c\}_j^1 = [K_{cf}]_{j-1}^0 \{du_f\}_j^1 + [K_{cc}]_{j-1}^0 \{du_c\}_j^1 - \{dF_c\}_j^1 \quad (22b)$$

Step 2: Update nodal displacement values

$$\{\mathbf{u}\}_j^1 = \{\mathbf{u}\}_{j-1} + \{du\}_j^1 \quad (23)$$

For the following steps of the analysis, expressions are valid for both first increment ( $k = 1$ ) and iterations is needed (i.e.,  $k \geq 2$ ) as explained later; thus the superscript in the expressions is used as  $k$ .

Step 3: For each cable-beam element  $b$ , the following relation holds:

$$\{u\}_{b,j}^k = [A]_b \{\mathbf{u}\}_j^k \quad (24)$$

where  $[A]_b$  is a matrix that relates the coupling between the cable-beam element  $b$  and rope degrees of freedom. Based on the assumption that lateral deflections are small, it is assumed that helical geometry of the strands is preserved; thus, their updated equivalent helix angles can be estimated as follows:

$$\tan(\beta_{s,j}^k)_b = \frac{2\pi(r_{s,j}^k)_b}{(p_s)_j} \quad (25)$$

where  $(p_s)$  is the updated pitch distance of the strands along the rope's length that for this particular rope construction is given by  $(p_s)_j = p_0(1 + u_{0,j}/L_{j-1})$  in which  $p_0$  is the initial pitch distance value;  $u_{0,j}$  is the total axial displacement of the rope at the  $j$ th step of the analysis; and  $r_{s,j}^k$  is the equivalent helix radius of the each strand assessed as  $r_{s,j}^k = r_{s,j-1} + d\Delta_{b,j}^1$  in which the latter is the increment in lateral deflection, considering both planes, of the cable-beam element  $b$ . The curvature of each strand can be estimated as

$$(\kappa_{s,j}^k)_b = \frac{(\sin(\beta_{s,j}^k)_b)^2}{(r_{s,j}^k)_b} \quad (26)$$

Step 4: The axial strain of each strand that forms cable-beam element  $b$  is computed based on Eqs. (6), (7), and (A.5–10), in which only the linear term of the Green strain tensor is retained

$$(\varepsilon_{s,j}^k)_b = [[N_u]^T - y_s [N_{\partial z}]^T + z_s [N_{\partial y}]^T] \{u\}_{b,j}^k (\cos(\beta_{s,j}^k)_b)^2 + \sqrt{y^2 + z^2}_s [N_{\partial x}]^T \{u\}_{b,j}^k \sin(\beta_{s,j}^k)_b \cos(\beta_{s,j}^k)_b \quad (27)$$

where the notation  $(\cdot)' = d(\cdot)/dx$  is used for the first derivative. Based on the updated geometry of each cable-beam element  $b$  and Eq. (27), their lengths are updated  $L_{b,j}^k = L_{b,j-1} (1 + (\varepsilon_{s,j}^k)_b |_{y_s=z_s=\beta_s=0})$  along with the transformation matrices  $[T]_{b,j}^k$  based on their direction cosines ([39]).

Step 5: The normal stress for the unbroken strands that form cable-beam element  $b$   $(\sigma_{s,j}^k)_b$  is calculated using their constitutive law considering their centroids as the generic point (i.e., one point integration). Based on previous works ([21,40]; among others), for the particular case of polyester, a polynomial function up to the fifth degree is used to express the normal stress of a generic point as a function of its axial strain, having the following form:

$$(\sigma_{s,j}^k)_b = \sigma_{smax} \left[ \sum_{t=1}^5 \tau_t \left( \frac{(\varepsilon_{s,j}^k)_b}{\varepsilon_{smax}} \right)^t \right] \quad (28)$$

where the coefficients  $\tau_t$  are constitutive parameters that are chosen to provide a best fit to measured data for polyester strands; and  $\sigma_{smax}$  and  $\varepsilon_{smax}$  are the breaking normal stress and strain of tested strands respectively.

Step 6: Internal nodal forces for each cable-beam element  $b$  can be

approximated by

$$\{F\}_{b,j}^k = \{F\}_{b,j-1} + [K_t]_{b,j-1} \{du\}_{b,j}^k \quad (29)$$

where  $\{F\}_{b,j-1}$  is the internal force vector for the cable-beam element at the end of the  $(j-1)$  step of the analysis and  $\{du\}_{b,j}^k$  is defined in Eq. (9). The residual load vector  $\{R\}_j^k$  is computed as

$$\{R\}_j^k = \{S\}_j^k - \{F\}_j^k \quad (30)$$

where  $\{S\}_j^k$  is the vector of equivalent nodal external forces applied obtained from Eqs. (C.2) and (C.3) (Appendix C) and  $\{F\}_j^k$  is the vector of net internal forces obtained by summing the existing cable-beam element end forces (based upon Eq. (29)) at each global degree of freedom using a standard assembly procedure of structural analysis as previously stated. If the norm of the residual load vector  $\{R\}_j^k$  (i.e.,  $\|\{R\}_j^k\|$ ) is less than a prescribed tolerance (*tol*) ( $1E-5$  used in this study), the damaged rope is in equilibrium and a new analysis is performed for the  $(j + 1)$ th increment in axial displacement  $du_{j+1}$  (Step 1).

**Step 7:** If  $\|\{R\}_j^k\| > tol$ , iterations on unknown variables in Eq. (21) are needed. For performing iterations (i.e.,  $k \geq 2$  in Eq. (15)), consider the following increments of the nodal load vectors. The nodal forces for each cable-beam element  $b$ ,  $\{Q\}_{b,j}^k$  and  $\{P\}_{b,j}^k$  are updated based on its updated geometry and axial load developed. For a generic cable-beam element  $b$ , the following expressions hold:

$$(q_{y,b})_j^k = [(\kappa_s)_{j-1} A_s (\sigma_{s,j}^k)_b \sqrt{G_1^2 + G_2^2 - 2G_1 G_2 \cos \alpha}]_b \cos \varphi \quad (31a)$$

$$(q_{z,b})_j^k = [(\kappa_s)_{j-1} A_s (\sigma_{s,j}^k)_b \sqrt{G_1^2 + G_2^2 - 2G_1 G_2 \cos \alpha}]_b \sin \varphi \quad (31b)$$

$$\{Q\}_{b,j}^k = \int_{L_b} [N_{\theta_z}]^T (q_{y,b})_j^k d\xi \quad (32a)$$

$$\{P\}_{b,j}^k = \int_{L_b} [N_{\theta_y}]^T (q_{z,b})_j^k d\xi \quad (32b)$$

$$\{dQ\}_{b,j}^k = \{Q\}_{b,j}^k - \{Q\}_{b,j}^{k-1} \quad (33a)$$

$$\{dP\}_{b,j}^k = \{P\}_{b,j}^k - \{P\}_{b,j}^{k-1} \quad (33b)$$

and the following system of equations is solved:

$$\begin{bmatrix} [K_{ff}] & [K_{fc}] \\ [K_{cf}] & [K_{cc}] \end{bmatrix}_{j-1}^0 \begin{Bmatrix} \delta(du_f) \\ \mathbf{0} \end{Bmatrix}_j^k = \begin{Bmatrix} \mathbf{0} \\ \delta(dB_c) \end{Bmatrix}_j^k + \begin{Bmatrix} \delta(dF_f) \\ \delta(dF_c) \end{Bmatrix}_j^k + \begin{Bmatrix} R_f \\ R_c \end{Bmatrix}_j^{k-1} \quad (34)$$

where the  $\delta()$  operator is associated with the variations of the increments of the corresponding variables. The above system of equations accounts for the fact that  $\delta(du_c)$  vanishes considering that the numerical algorithm proposed is based upon the displacement control analysis procedure. Solving the above system of equations yields

$$\{\delta(du_f)\}_j^k = [[K_{ff}]_{j-1}^0]^{-1} \{\delta(dF_f)\}_j^k + \{R_f\}_j^{k-1} \quad (35a)$$

$$\{\delta(dB_c)\}_j^k = [K_{cc}]_{j-1}^0 \{\delta(du_f)\}_j^k - \{\delta(dF_c)\}_j^k - \{R_c\}_j^{k-1} \quad (35b)$$

where the tangent stiffness matrix of the damaged rope  $[K_{dr}]$  is kept constant during iterations, as it is seen in the submatrices  $[K_{ff}]$ ,  $[K_{fc}]$ ,  $[K_{cf}]$ , and  $[K_{cc}]$  in Eq. (34), and it is updated at the end of each increment.

**Step 8:** Update nodal displacement values

$$\{u\}_j^k = \{u\}_j^{k-1} + \{\delta(du)\}_j^k \quad (36)$$

Repeat from Step 3 to Step 8 until the condition  $\|\{R\}_j^k\| \leq tol$  is achieved, in which iteration variable increases from  $k$  to  $k + 1$ .

The above numerical algorithm is quite general except for the computation of the increment in nodal forces  $dQ_{b,j}^k$  and  $dP_{b,j}^k$  in Steps 1 and 7 which depend on the type of cross-section construction analyzed. Nevertheless, regardless the latter particularity, their values rely on the application of the radial equilibrium equation considering the contact line forces between rope components whose values depend on their

curvatures and tensile forces when treated as thin curved fiber elements. As such, constitutive law of rope components is needed for this purpose (Step 5). A flowchart of the proposed algorithm is provided in Appendix E.




#### 4. Numerical results and discussion

As previously mentioned, data on large-scale polyester asymmetrically damaged ropes reported in [10] are used to study and evaluate the coupled effect of strain localization and asymmetry in damage distribution phenomena on damaged rope response including the impact on rope stiffness, reduction in rope strength and deformation capacity, strain/stress field distribution, and rope deformed configuration. Tested ropes have undamaged specified breaking strength (SBS) values of 35 tonnes (343.2 kN) and 700 tonnes (6864.6 kN), with diameters that vary from 32 mm to 166 mm, and initial damage level of rope cross-section ranging from 5% to 15%. The reported data correspond to the last step of the test procedures conducted by [10]: capacity tests of damaged ropes. Previous steps carried out are bed-in the ropes, inflict prescribed damage level at ropes midspan, and cycle the ropes to simulate storm loading. As in previous works ([13,20,21]), the degree of asymmetry of the damaged cross-section is captured by a scalar quantity termed the index of asymmetry (*IA*). This parameter accounts for the shift of the center of stiffness of the damaged cross-section relative to the intact rope cross-section due to the asymmetric distribution of damage. For computational purposes, the initial value of this parameter ( $IA)_0$  (computed for small rope axial strain value) is considered as a representative measure of the degree of asymmetry of the rope cross-section (hereafter referred to as *IA*) as extensively discussed in [20].

Numerical simulations consider the constitutive laws of the strands that form the ropes (Step 5 of the Section 3.2 Numerical algorithm procedure) obtained from undamaged rope test data using the procedure proposed in [4] and validated in [23]. The boundary conditions for numerical simulations consider one end section of the ropes fully clamped and at the other end an axial displacement history is specified and the cross-section is prevented from rotating (Fig. 4). In Table 1, damaged cross-section, geometry, breaking load, and parameters associated to the numerical proposed model (damage level, index of asymmetry, and recovery length among others) of the different types of rope constructions analyzed in this study are shown in which broken strands are colored black. According to the report given in [10], prior performing capacity tests of damaged ropes, rope jackets were damaged (in order to inflict damage to rope specimens) and loose around damage area. Hence, the computation of the recovery length values, based on the description presented in Section 3.1, assumes relative small axial capacity and thickness values of each rope jacket that range from 0.5% to 1% of the initial undamaged strength and 2% of the diameter value of its corresponding rope respectively and a friction coefficient ( $\mu$ ) equal to 0.1, as extensively discussed in [19]. The results presented in the following correspond to the subsequent ropes discretizations based on the value of the  $L/d$  parameter ( $L$  and  $d$  are the rope's length and rope's diameter respectively) and the recovery length values for each rope listed in Table 1: ten cable-beam elements along the strain localization region and one cable-beam element for the region where all the strands contribute to rope response (if broken strands fully develop their recovery length values). The estimated helix angles values ( $\beta_s$ ) for the strands that form these ropes are  $12^\circ$  for ropes R1 and R2 and  $10^\circ$  for rope R3 for both SBS values.

In order to illustrate the coupled effect of strain localization and asymmetry in damage distribution on damaged rope response, the strain distribution within rope cross-section for the types of ropes R1, R2, and R3 with a SBS value equal to 35 tonnes is presented at three locations along their longitudinal axes considering an initial damage of 10% of the total cross-sections and an  $L/d$  parameter equal to 1000, in which all the locations are within the strain localization zone as depicted in Fig. 5. One of these corresponds to a cross-section of the cable-

**Table 1**  
Types of rope constructions.

Rope	SBS (kN)	Rope diameter (mm)	Initial damage level (%)	Index of asymmetry ( $IA$ )	Recovery length (mm)
R1 	343.2 6864.6	32 160	[5-10]	[0.1-0.16]	690 3230
R2 	343.2 6864.6	32 147	[5-10]	[0.19-0.3]	870 2950
R3 	343.2 6864.6	36 166	[10-15]	[0.17-0.27]	710 3050

beam element where initial damage was inflicted (initially broken strands colored black); thus, the maximum effect of asymmetry in damage distribution on strain field is expected. The other two locations correspond to cable-beam elements also in the recovery length region whose broken strands have partially developed their recovery length values; hence, asymmetry in damage distribution and consequently the index of asymmetry of the cross-section along with the unbalanced transverse sinusoidal load diminish. Based on the results presented in this figure, common conclusions for all the rope types analyzed can be drawn: strain localization develops around failure region, asymmetry in damage distribution induces a gradient in strain distribution in which maximum strains develop adjacent to damage and minimum strains opposite to it; and gradient in strain distribution throughout damaged cross-sections decreases as the broken strands resume carrying their proportionate share of axial load due to frictional effects.

In particular, outside of the recovery length region, it is expected that axial strain values of cable-beam elements converge to the axial strain ( $\epsilon_{rope}$ ) specified for the rope (intact case) as the ratio between recovery length ( $r$ ) and rope's length ( $L$ ) gets smaller [23]. Thus, the axial strain of the rope strands ( $\epsilon_s$ ) is given by  $\epsilon_s = \epsilon_{rope}(\cos\beta s)^2$ . In Table 2, a summary of maximum strain develop ( $\epsilon_{smax}$ ) in the most strained section of the rope and the ratios  $r/L$ , between maximum and minimum strain values within of the most strained rope cross-section ( $f_1$ ), and between maximum strain and strain expected outside the recovery length region values ( $f_2$ ) for each rope analyzed is provided. Rope types R1 and R2 have the same diameter (32 mm) and similar number of subropes (24 and 18, respectively) and initial  $IA$  values (0.16 and 0.19 respectively) showing a comparable (around 15%) maximum increment in axial strain value relative to the intact case in the strain localization region. Conversely, although rope type R3 has similar initial  $IA$  value than previous ropes (0.17), it has fewer number of subropes (10) and greater diameter (36 mm) inducing smaller maximum increment in axial strain value relative to the intact case in the strain localization region (around 8%). It is important to point out that if only the strain localization phenomenon were accounted for,  $f_2$  values would reduce to  $f_{2SLM}$  values (Table 2); thus, the effect of asymmetry in damage distribution and its interaction with the strain localization phenomenon on the maximum strain developed is 4% for ropes R1 and R2, and 0.9% for rope R3. This analysis corroborates previous works in finding that the dominant phenomenon that rules static response of these ropes is the strain localization ([10,19,23]).

In terms of the stiffness, residual strength, and deformation capacity (i.e., capacity curves) of the damaged ropes previously analyzed, it is important to have in mind that one of the conclusions drawn in [23] was to prove that acting independently, using two numerical algorithms that independently account for the strain localization ( $SLM$ ) and asymmetry in damage distribution ( $ADDM$ ) mechanisms, they bound damaged rope response (experimental curves): upper and lower bounds associated to strain localization and asymmetry in damage distribution phenomena, respectively which is illustrated in Fig. 6. In this figure, the solution space of damaged rope is given by the shaded area between the  $SLM$  (upper bound) and  $ADDM$  (lower bound) curves in the axial load-axial strain plane. As a reference, the virgin rope response and net area (damaged rope response obtained solely from unbroken rope components contribution) curves are also included in the plot to show that  $SLM$  and  $ADDM$  curves eventually converge to them respectively, with a reduction in load carrying and axial deformation capacities of the ropes.

In respect of the analysis of capacity curves, measured data reported in [10] are compared with the following predicted curves:  $SLM$  and  $ADDM$  that limit the solution space of damaged rope response and  $NLCBM$  that couples the strain localization and asymmetry in damage distribution considering the formulation presented in Sections 2 and 3. In this way,  $NLCBM$  is validated and the corresponding simulations are used to interpret and extend the measured data. For the tests of ropes with SBS equal to 35 tonnes, different  $L/d$  ratio were considered (ranging from 40 to 1000) to try to evaluate the dependency on this parameter of damaged rope response; thus  $NLCBM$  curves account for this parametric variation, although as  $L/d$  increases,  $NLCBM$  simulations converge to unique curve as discussed in [41]. In addition, measured and predicted curves of intact ropes are shown for reference purposes.

In Fig. 7, measured and predicted capacity curves of ropes R1, R2, and R3 with an SBS value equal to 35 tonnes and initial damage level of 10% of the cross-section asymmetrically distributed are presented. Although tested ropes have different types of constructions but the same initial damage level,  $IA$  values associated to the initial inflicted damage distribution vary in a narrow range from 0.16 to 0.19.

For the case of rope type R1 (Fig. 7a),  $NLCBM$  curves coincide with  $SLM$  curve for small values of axial strain (less than 0.035). For greater strain values,  $NLCBM$  curves slightly deviate from the  $SLM$  curve mainly due to the bending effect induced by the asymmetry in damage distribution (i.e.  $NLCBM$  curve falls inside of the solution space (Fig. 6)).



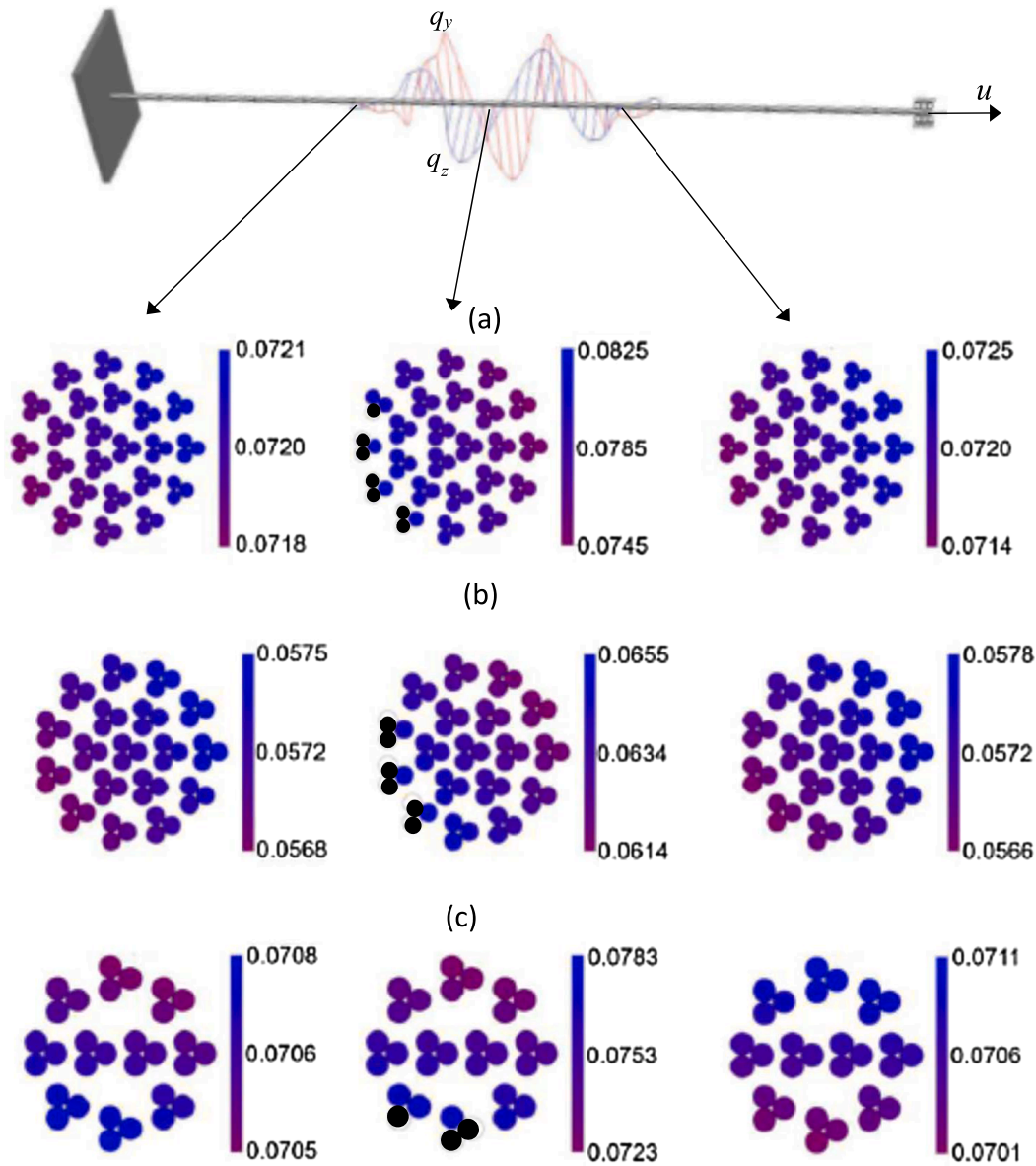


Fig. 5. Effect of strain localization and asymmetry in damage distribution on strain field. Rope types with SBS = 35 tonnes: (a) R1, (b) R2, and (c) R3.

Table 2

Summary of the increment in axial strain due to the coupling of strain localization and asymmetry in damage distribution phenomena. Ropes with SBS = 35 tonnes.

Rope	$[r/L]\%$	$(\epsilon_{rope})$	$(\epsilon_{smax})$	$f_1$	$(\epsilon_s)$	$f_2$	$f_{2SLM}$
R1	2	0.075	0.0825	1.11	0.71	1.16	1.11
R2	3	0.06	0.0655	1.07	0.057	1.15	1.10
R3	2	0.075	0.0783	1.08	0.072	1.08	1.07

According to [10], Exp. 2 ( $L/d = 290$ ) failed at one end splice probably due to a stress concentration that made that the rope response fell outside of the solution space. These curves experience a stiffening process that is well captured by the corresponding *NLCBM* curves, especially for Exp. 1 and Exp. 3 curves. *NLCM* curves, however, underestimate the measured residual strength and deformation capacity values in the ranges of [4%, 12%] and [5%, 10%] respectively.

Regarding the case of rope type R2 (Fig. 7b), both tested ropes ( $L/d = 290$  and 1000) failed near the initially damaged region as reported in [10]. Exp. data 2 ( $L/d = 1000$ ) curve falls outside of the solution

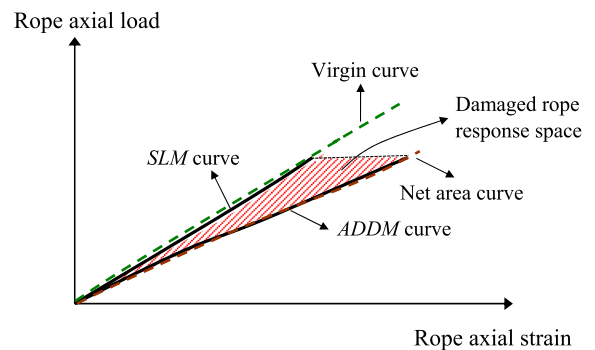


Fig. 6. Solution space of damaged rope response.

space because additional strands failed during simulation of storm loading increasing the cross-sectional damage from 10% to 17%. Moreover, this rope response was mainly governed by the asymmetry in damage distribution phenomenon associated to a damage level equal to 17% ([23]). On the other hand, the *NLCBM* ( $L/d = 290$ ) curve accounts

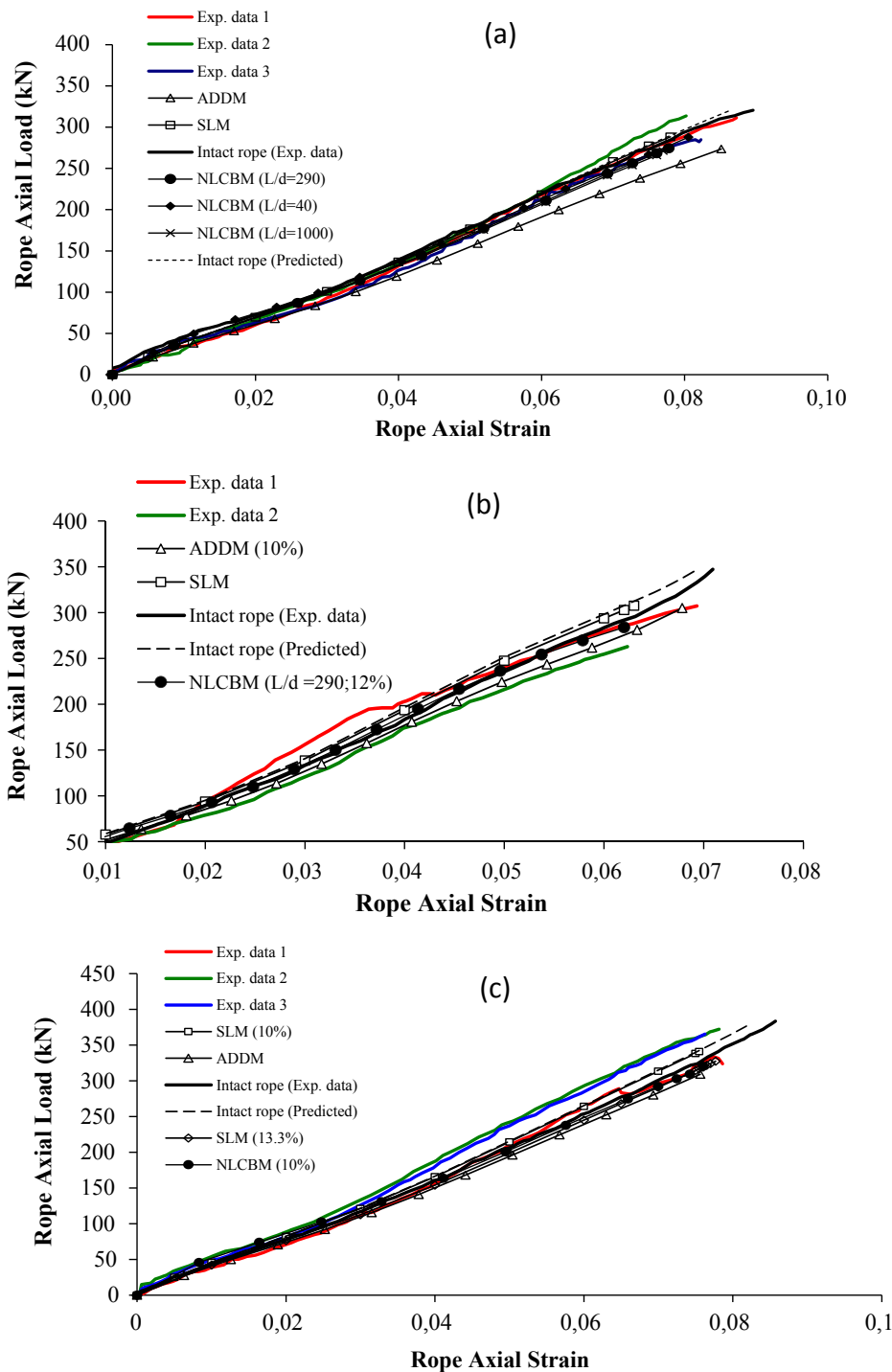


Fig. 7. Capacity curves of initially damaged ropes with SBS equal to 35 tonnes: (a) type Rope R1; (b) type Rope R2 and (c) type Rope R3.

for an initial damage equal to 12% of the rope cross-section due to the individual strand failures during the experiment (Exp. Data 1 ( $L/d = 290$ )) as detailed in [10]. *NLCBM* ( $L/d = 290$ ) curve falls in the solution space approaching to its upper bound. Exp1 is somewhat stiffer than the *SLM* curve (upper bound) in the axial strain range [0.025, 0.04] after which it softens converging to the *NLCBM* curve in the range [0.045, 0.062], and based on the testing report, failing at cut location. The *NLCBM* ( $L/d = 290$ ) predicts an earlier rope failure underestimating the experimental residual strength and deformation capacity values in 7% and 10% respectively.

Finally, for the case of rope type R3 (Fig. 7c), Exp. data 3 ( $L/d = 590$ ) and Exp. data 2 ( $L/d = 1000$ ) curves are stiffer than the *SLM*

curve (upper bound) falling outside of the solution space probably due to stress concentration near one splice and unwinding process [10,23]. For the case of Exp. data 1 ( $L/d = 40$ ) curve, its behavior is well captured by the *SLM* considering two damage levels: 10% and 13.3%. The latter is due to some strands failure at strain value equal to 0.07, according to [10,23]. The *SLM* (13.3%) curve underestimates the measured residual strength and deformation capacity by less than 0.5%, suggesting that strain localization phenomena rules rope response and the effect of asymmetry in damage distribution is negligible. It is believed for this case, that as the rope length gets shorter ( $L/d = 40$ ), strain localization is induced by rope terminations along with rope jacket confinement. The proposed model (*NLCBM*) does not capture

properly the boundary condition effects on strain localization and kinematics of deformation of the rope (bending deformation is restricted by end splices) as extensively discussed in [41].

Based on the predicted and measured capacity curves presented in Fig. 7 along with previous studies ([10,19,23]), it is not clear how the response of a damaged rope depends on the  $L/d$  parameter; hence, no conclusive findings can be drawn. In general, measured data and simulations provided by the *NLCBM* indicate that the residual strength depends on the type of rope construction: as the  $L/d$  parameter decreases, measured and estimated residual strength decrease as well for rope type R1 providing minimum values smaller than the ones predicted by the net area effect (90% of the virgin value) with a maximum deviation equal to 5%; estimated values moderately decrease for rope type R2 and they are essentially constant for the rope type R3; and for both rope types, estimated residual strength values are slightly smaller than values predicted by the net area effect. If only the strain localization phenomenon were considered in the analysis, estimated residual strength values would match with the ones provided by the net area effect ([23]); hence, deviations observed in the analysis are due to the presence of the asymmetry in damage distribution phenomenon and its nonlinear coupling with the strain localization one. Measured data of the residual strength for the R2 and R3 rope types, however, fluctuate not showing a definite trend as the  $L/d$  value increases. For the deformation capacity values case, for all rope types as the  $L/d$  value increases, estimated (*NLCBM*) values decrease. The maximum reduction relative to the virgin case is similar to the initial damage level inflicted to ropes (10%). Measured values, however, show different behavior depending on the type of rope construction as the  $L/d$  value decreases: (1) R1 values fluctuate not showing a definite trend; (2) R2 values remain constant for the first two  $L/d$  values for later decrease ( $L/d = 1000$ ); and (3) R3 values are primarily constant and the reduction in deformation capacity relative to the virgin case is close the damage level inflicted to ropes (10%) prior performing ropes capacity tests, comparing well with the predicted one for  $L/d = 1000$ . Based on this analysis, it seems that measured values appear to be strongly influenced by different mechanisms that potentially stiffen rope response such as unwinding, stress concentration near ropes ends, and jacket confinement ([10,23]). More experimental data is needed to evaluate the dependency of damaged rope response on the  $L/d$  parameter, considering different types of rope constructions, damage distribution, damage level to rope cross-section, and rope sizes.

In order to establish the robustness of *NLCBM*, bigger damaged ropes are analyzed (SBS equal to 700 tonnes) with a fixed value of the parameter  $L/d$  ( $L/d = 40$ ). Based on the recovery length values presented in Table 1, broken strands of ropes R1 and R2 partially contribute to rope response because ropes lengths are not long enough to allow them to fully develop their recovery length values, although symmetry in axial strain distribution within ropes cross-sections is expected to be reached in sections toward the ropes ends (Fig. 8a). Consequently, strain localization and asymmetry in damage distribution phenomena are present along the entire ropes. This fact is illustrated in Fig. 8b, c, for ropes R1 and R2 respectively based on the rope discretization (the same for both ropes) depicted in Fig. 8a, considering a 10% of their cross-sections damaged. Similar to the information summarized in Table 2 for smaller ropes, the analysis of the aforementioned ropes is given in Table 3. Larger  $f_2$  value is obtained for the R1 rope although both damaged ropes have similar  $IA$  values (around 0.17). This is probably due to the fact that R1 rope diameter (160 mm) is greater than the one associated to rope R2 (147 mm); thus bending effect (associated to the corresponding lever arm) on strain distribution is bigger.

As in the case of ropes with SBS equal to 35 tonnes, if solely the strain localization phenomenon were considered,  $f_2$  (referred as  $f_{2SLM}$ ) would be 1.09 and 1.08 for ropes R1 and R2 respectively (Table 3). Hence, the effect of asymmetry in damage distribution and its interaction with the strain localization phenomenon on the maximum strain

developed is 3.5% and 1.8% for the aforementioned ropes respectively. These values are of the same order as those obtained for the same type of ropes with SBS equal to 35 tonnes. These relative marginal contributions to the maximum strain developed in each cross-section, is a strong evidence that the response of these damaged ropes is also mainly ruled by the strain localization phenomenon.

An interpretation of the measured damaged rope responses for the aforementioned bigger ropes, described in Table 1, is given in Fig. 9 based on their comparisons with predicted responses obtained from numerical models (*NLCBM*, *SLM*, and *ADDM*). Conversely to the ropes R1 and R2 previously discussed, broken strands of rope R3 completely recover their proportionate share of axial loads concentrating the coupled effect of asymmetry in damage distribution and strain localization phenomena around the initial fracture region (rope midspan).

For the case of rope type R1 (Fig. 9a), the initial inflected damaged to rope cross-section was equal to 5% distributed in two subropes, inducing an  $IA$  value equal to 0.1. The *NLCBM* curve falls in the solution space (close to the *SLM* curve) suggesting that the rope response is mainly governed by the strain localization phenomena. This curve slightly deviates from the *SLM* curve as the axial strain values greater than 0.045 due to the bending deformation induced by the asymmetry in damage distribution. Although the Exp. data curve is a little stiffer than the latter one in some interval of the strain range, it softens converging to the *NLCBM* for axial strain values greater than 0.07, showing an earlier failure than the predicted one. The *NLCBM* curve overestimates the measured residual strength and deformation capacity values in 8% and 5% respectively. For the case of rope type R2, the initial damage inflicted to rope cross-section was equal to 10%. Exp. data curve shows some individual strand failures that soften its response prior to its complete rupture, increasing its damage level to 20% distributed to five subropes and  $IA$  value from 0.17 to 0.3 ([23]). After the individual strand failures occurred (strain greater than 0.05), Exp. data curve is bounded by the *SLM* (20%) and *NLCBM* (20%) in a narrow region in which the latter falls in the solution space and underestimates the measured residual strength and deformation capacity in 6% and 3% respectively (Fig. 9b). For low strain values (less than 0.025), Exp. data curve matches well with the *ADDM* (10%) curve, after which the former experiences a stiffening process which results in a slightly stiffer response than the upper bound curve that ends up with the individual strand failures previously commented. According to [10], this specimen failed at the rope midspan where initial damage was inflicted.

In Fig. 9c, estimated and measured capacity curves of rope type R3 with a 15% of initial damage level is presented. An individual strand failure occurred during the execution of the tensile test (at axial strain value equal to 0.05) increasing the damage level to 18% and  $IA$  value from 0.25 to 0.27 ([23]). *NLCBM* (18%) curve falls in the solution space and compares quite well with Exp. data curve from low strain values suggesting that strain localization phenomenon rules damaged rope response as the *SLM* (18%), intact rope (measured and predicted), and *NLCBM* (18%) curves coincide. Slight deviation between *NLCBM* (18%) and Exp. data curves is seen within the axial strain range [0.04, 0.05] in which the latter gets stiffer, but after the individual strand failure, both curves match well again between each other. The *NLCBM* (18%), however, predicts an earlier rope rupture underestimating the measured residual strength and deformation capacity in 14% and 12% respectively, due to a potential unwinding process experienced by the tested rope ([10,23]).

Lastly, the deformed configurations of two of the rope constructions considered in this study are shown in Fig. 10. Two axial rope strains are examined for the case of rope R1 with SBS equal to 35 and 10% of cross-sectional damage: 0.026 and 0.078 (Fig. 10a), in which the latter corresponds to the rope axial strain at the onset of its failure. A value of  $L/d$  equal to 290 is used for computations purposes; hence, broken strands fully develop their recovery length values as previously commented which is reflected in the straight rope configuration outside the recovery length region. Inside of the recovery length region of the rope

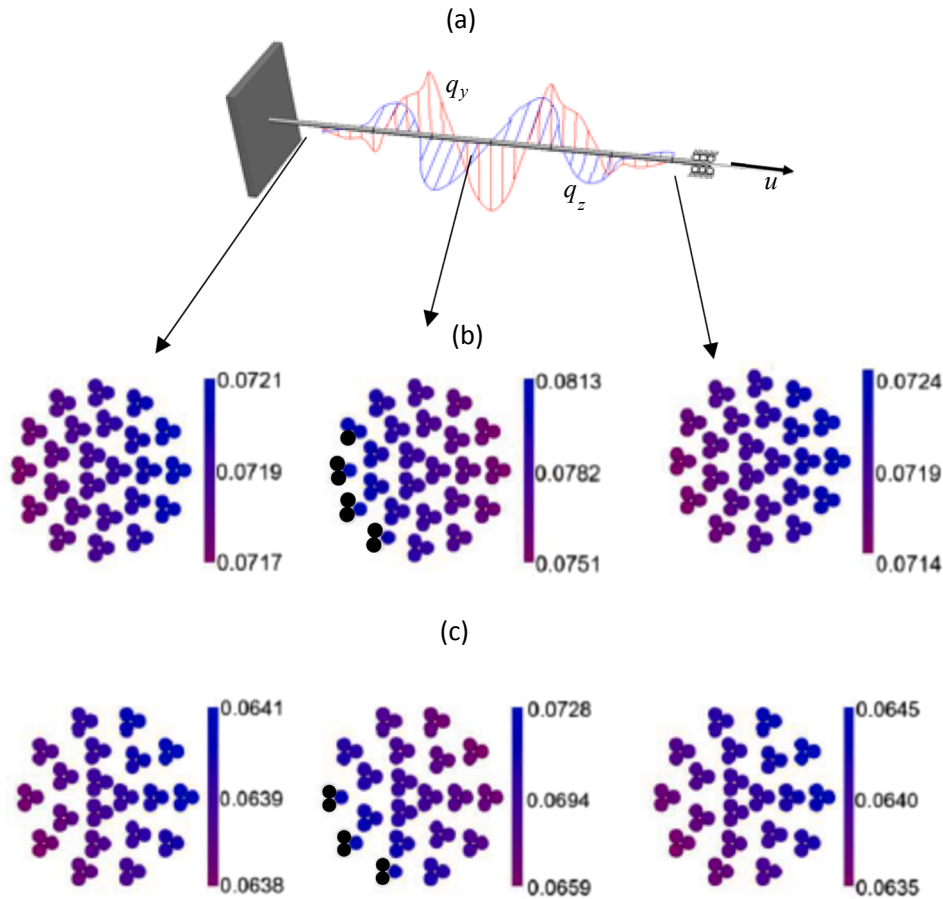


Fig. 8. (a) Ropes discretization; (b) and (c) Strain distributions for damaged ropes R1 and R2 respectively (SBS = 700 tonnes).

Table 3

Summary of the increment in axial strain due to the coupling of strain localization and asymmetry in damage distribution phenomena. Ropes with SBS = 700 tonnes.

Rope	$[r/L]\%$	$(\epsilon_{rope})$	$(\epsilon_{smax})$	$f_1$	$(\epsilon_s)$	$f_2$	$f_{2SLM}$
R1	50	0.075	0.0813	1.08	0.71	1.13	1.08
R2	50	0.069	0.0728	1.10	0.066	1.10	1.09

(around rope midspan), the value of the maximum net unbalanced line force  $q_R$  ranges from 0 to 650 kN/m (upper bound value associated to a rope axial strain equal to 0.078) inducing a slight lateral deflection of the rope following an inclined helix curve with decreasing amplitude as the asymmetry of rope cross-section diminishes (Fig. 10a). The maximum lateral deflection is captured by the closest cable-beam element to the rope midspan which corresponds to 0.2% and 0.7% of the rope diameter (32 mm) for both rope axial strain values (0.026 and 0.078) respectively. On the other hand, the deformed configuration of rope R2 with SBS equal to 700 tonnes and 20% of cross-sectional damage is depicted in Fig. 10b for the axial strain values equal to 0.021 and 0.062. The initial  $L/d$  ratio considered is equal to 40; hence, as discussed in Fig. 9b, broken strands partially contribute to rope response and asymmetry of rope cross-section and rope lateral deflection along its entire length gets smaller as approaching to rope ends. For both rope axial strain values selected (0.021 and 0.062), in which as in the previous case the latter corresponds to the axial strain at the onset of rope failure, the maximum lateral deflection located at rope midspan is equal to 0.5% and 1.3% of the rope diameter (147 mm) respectively, which is induced by the net unbalanced line force  $q_R$  whose maximum values range from 0 to 2570 kN/m. This rope deflection, which is basically an

inclined helix with decreasing amplitude, slightly perturbs the initial rope straight configuration.

According to the analyses presented in this study that consider particular types of rope constructions, damage levels, and damage distributions, in most of the cases analyzed strain localization phenomenon rules damaged ropes response, fact that is well captured by the *NLCBM*. As such, the Bernoulli's kinematic hypothesis is accurate enough to capture the bending strains induced in the rope due to the asymmetry in damage distribution and the assumptions over which the procedure proposed to estimate recovery length values relies on are reasonable. Experimental curves reveal, however, that this phenomenon takes place gradually as the ropes are stretched, being the net area effect (captured by *ADDM*) the one that prevails at the early stages (small axial strain values) of damaged ropes response. It is important to point out that *NLCBM* shows to be robust and computationally efficient. Its robustness is asserted with the fact that *NLCBM* is able to interpret and simulate measured capacity curves of damaged ropes considering a wide range of rope sizes, damage levels, asymmetry in damage distribution, and different types of rope construction. As to the computational efficiency, the *NLCBM* requires few iterations to converge at each step of the analysis (Step 7 of the numerical algorithm procedure (Section 3.2)).

### 5. Final remarks

In this paper, the coupled effects of strain localization and asymmetry in damage distribution on damaged rope response were studied. To this end, a robust and a numerical efficiency algorithm is proposed that relies on the finite element method in which a damaged rope is discretized along its length into 1D two-noded nonlinear cable-beam elements with six degrees of freedom (dof) per node and Bernoulli's

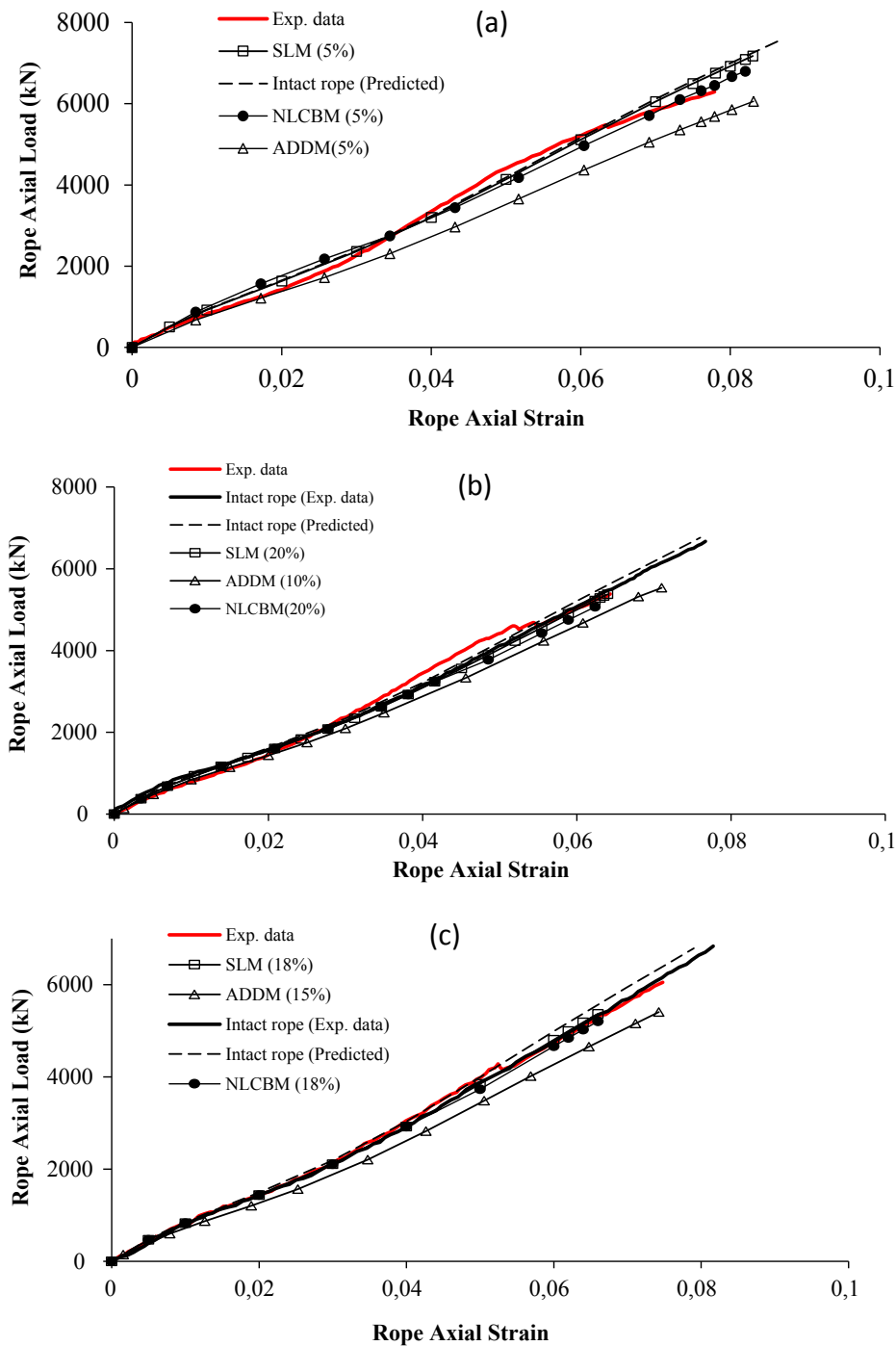


Fig. 9. Capacity curves of initially damaged ropes with SBS equal to 700tonnes: (a) type Rope R1; (b) type Rope R2 and (c) type Rope R3.

kinematic hypothesis. The proposed generic cable-beam element accounts for the helical structure of a rope (cable) as well as the axial-bending, axial-torsional, and bending-torsional interactions. For a particular analysis, capacity curve, axial strain field along rope’s length, and deformed configuration are obtained in less than five minutes on a standard multi-core processor laptop (Intel Core i7-16 Gb RAM).

The proposed numerical model (*NLCBM*) was validated by comparisons with experimental static capacity curves of large-scale damaged polyester ropes reported in [10]. The construction of the tested ropes consist of a group of parallel sub-ropes which are covered by a protective braided jacket, they have specified breaking stress values equal to 35 tonnes and 700 tonnes, their diameter values range from 32 mm to 166 mm, and initial asymmetrically distributed cross-

sectional surface damage values vary from 5% to 15%.

In terms of the numerical results provided by the *NLCBM*, estimated capacity curves of damaged ropes fall in the solution space for damaged rope response limited by the curves associated to strain localization (upper bound) and asymmetry in damage distribution (lower bound) phenomena acting separately. Good comparisons between estimated and measured static capacity curves of damaged ropes reveal that strain concentration phenomenon, induced by rope jacket confinement and/or ropes ends effect, and/or interactions between broken and unbroken rope components, rule damaged ropes responses in most of the cases analyzed. As a general conclusion, the nonlinear coupling of strain localization and asymmetry in damage distributing phenomena induces that the predicted reduction in the rope strength values be greater than

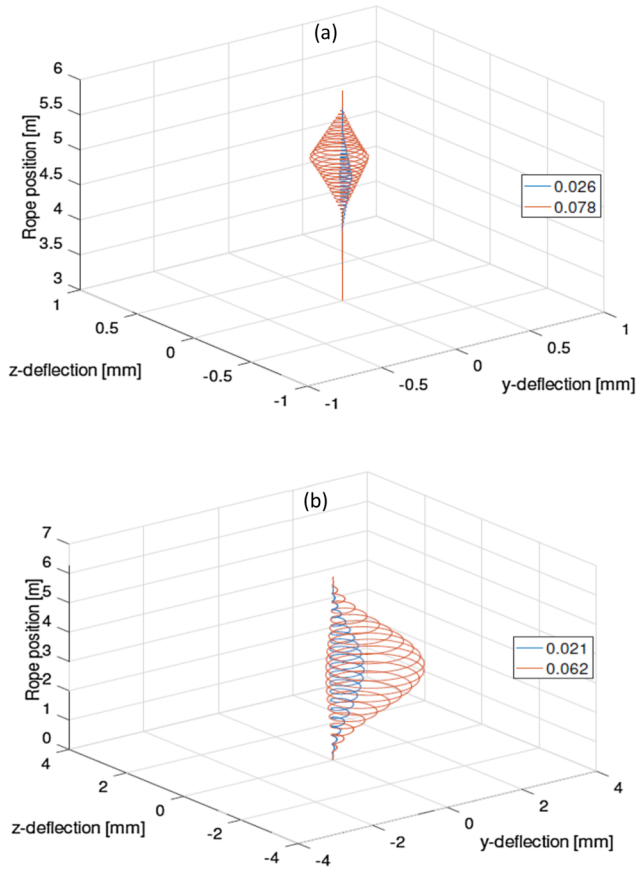


Fig. 10. (a) Deformed configurations: (a) rope type R1 with SBS = 35 tonnes 10% of damage; (b) rope type R2 with SBS = 700 tonnes 20% of damage.

the damage level (net area effect concept) with a maximum deviation from the latter equal to 6%; and for the case of the reduction in deformation capacity relative to the virgin case, predicted values are quite similar to the damage level inflicted to ropes cross-sections. Contrary, measured values, especially the reduction in rope strength, do not show a clear trend and they seem to be strongly influenced by different mechanisms that potentially stiffen rope response such as unwinding, stress concentration near ropes ends, and jacket confinement. More

### Appendix A. Approximation of kinematic variables

Expressions to compute  $[k_L]_b$ ,  $[k_G]_b$ ,  $\{f_{j-1}^j\}_b$ , and  $\{f_{j-1}^{j-1}\}_b$  associated to Eq. (9) based on the approximation of the kinematic variables ([33]):

$$\{\delta u\}_b^T [k_L]_b \{u\}_b = \int_{V_{j-1}} (E_t)_{j-1} \Delta e_j \delta_{j-1} e dV_{j-1} \tag{A.1}$$

$$\{\delta u\}_b^T [k_G]_b \{u\}_b = \int_{V_{j-1}} \sigma_{j-1} \delta_{j-1} \eta dV_{j-1} \tag{A.2}$$

$$\{\delta u\}_b^T \{f_{j-1}^j\}_b = F_{j-1}^j \tag{A.3}$$

$$\{\delta u\}_b^T \{f_{j-1}^{j-1}\}_b = F_{j-1}^{j-1} \tag{A.4}$$

where  $\{\delta u\}_b$  corresponds to the virtual nodal displacements vector of the cable-beam element, obtained by applying the operator  $\delta()$  to  $\{u\}_b$  (Eq.5). The displacement functions of a standard two-noded cable-beam element in a 3D-space are approximated as follows in terms of the kinematic variables  $\{u\}_b$  (Eq. (5)):

$$u(x) = N_1 u_t + N_2 u_f = [N_u] \{u\}_b \tag{A.5}$$

$$\theta_x(x) = N_1 \theta_{xt} + N_2 \theta_{xf} = [N_{\theta_x}] \{u\}_b \tag{A.6}$$

experimental data is needed, considering different types of rope constructions, damage distribution, damage level to rope cross-section, and rope sizes, to determine the influence of previous parameters on the reduction of rope strength and rope deformation capacity. Although, the static response of the tested ropes is mainly governed by the strain localization phenomenon, asymmetry in damage distribution induces additional local bending strains along the length over which damage propagates in the rope: a gradient in strain distribution within damaged rope cross section is engendered in which maximum axial strains develop adjacent to damage and rope deflects laterally. Numerical simulations of tested ropes suggest that maximum strain gradient values are in the range of [7%, 11%] and the maximum increments in strain values relative to the intact one vary from 7% to 16%. Regarding the deformed configuration of the ropes, their initial straight alignments are slightly perturbed laterally in which the maximum lateral deflection values are 0.7% and 1.3% of rope diameters for ropes with SBS equal to 35 tonnes and 700 tonnes respectively.

In spite of the good performance of the proposed computational tool (*NLCBM*) in interpreting experimental data and assessing damage-tolerance property of particular types of ropes, additional comparisons with other well-accepted numerical technique (e.g. 3D FEM) and experimental data of ropes comprised of diverse materials and construction types are needed to establish the range of applicability of the *NLCBM*. Although *NLCBM* formulation accounts for geometric and material nonlinearities and the helical nature of rope components, they are treated as tensile elements neglecting their transverse deformation and local bending and contact and frictional forces between them. In order to account previous effects that allow to simulate the complex interaction between rope components, including the potential relative slip between them due to changes in curvatures, a richer model that considers each rope component as a rod element needs to be explored. Regardless these limitations, and based on the preliminary results presented in this paper along with the computational efficiency and robustness, the proposed model seems to be a promising computational tool to interpret static experimental data and estimate rope service life at the design stage and to establish rope inspection methods and discard criteria according to rope usage.

### Acknowledgement

This work was supported by Fondecyt (Chile) Grant N° 1150409. The authors gratefully acknowledge this funding.

$$v(x) = N_3 v_I + N_4 v_J + N_5 \theta_{zI} + N_6 \theta_{zJ} = [N_{\theta_z}] \{u\}_b \quad (\text{A.7})$$

$$w(x) = N_3 w_I + N_4 w_J + N_5 \theta_{yI} + N_6 \theta_{yJ} = [N_{\theta_y}] \{u\}_b \quad (\text{A.8})$$

where  $[N_k]$  are row vectors of dimensions  $1 \times 12$  with interpolation functions  $N_i$  ( $i = 1, \dots, 6$ ) as components defined as

$$N_1(\xi) = \left(1 - \frac{\xi}{L}\right); N_2(\xi) = \frac{\xi}{L} \quad (\text{A.9})$$

$$N_3(\xi) = \left(1 - 3\left(\frac{\xi}{L}\right)^2 + 2\left(\frac{\xi}{L}\right)^3\right); N_4(\xi) = \left(3\left(\frac{\xi}{L}\right)^2 - 2\left(\frac{\xi}{L}\right)^3\right)$$

$$N_5(\xi) = \xi \left(1 - \frac{\xi}{L}\right)^2; N_6(\xi) = \xi \left(\left(\frac{\xi}{L}\right)^2 - \frac{\xi}{L}\right) \quad (\text{A.10})$$

where  $\xi$  refers to the local longitudinal axis of the two-noded cable-beam element.

### Appendix B. Damage level of cable-beam elements

Based on the finite element discretization of a damaged rope, each cable-beam element  $b$  exhibits a damage level  $D_s$  according to the position of this element  $b$  relative to  $rl$ . Let  $x$  be the longitudinal axis of the rope and assume that  $[0,rl]$  is the interval over which the recovery length fully develops along the damaged rope from the rupture region. The parameter  $\lambda = \lambda(\rho_b)$  is a function that quantifies the stiffness recovery level of broken strands due to frictional effects evaluated at the centroid ( $\rho_b$ ) of the element  $b$ . As such,  $\lambda_b(\rho)$  is defined as

$$\lambda_b(\rho_b) = \frac{rl(T_s(\rho_b))}{rl} \quad (\text{B.1})$$

where  $rl(T_s(\rho_s))$  is computed using Eqs. (11). The damage level of damaged strands in each cable-beam element  $b$ ,  $D_s(\rho_b)$ , is estimated as

$$D_s(\rho_b) = 1 - \lambda_b(\rho_b) \quad (\text{B.2})$$

where  $D_s = 1$  refers to a complete rupture and  $D_s = 0$  is the virgin state of the strand cross-section. Considering that damage level (or damage index)  $D_s$  is a dimensionless entity defined as the ratio between the damaged and virgin cross-sectional areas of the strands,  $A_{sd}/A_{sv}$ , ([42]), the expressions to compute the local linear  $[k_L]_b$  and geometric  $[k_G]_b$  stiffness matrices for each cable-beam element  $b$  for the  $j$ th increment of the analysis, considering a symmetric formulation, are given by

$$[k_L]_{b,j} = \begin{bmatrix} k_{L11} & \cdots & k_{L112} \\ \vdots & \ddots & \vdots \\ k_{L121} & \cdots & k_{L1212} \end{bmatrix}_{b,j} = \sum_{i=1}^{16} [k]_{(i,b)j} \quad (\text{B.3})$$

where

$$[k]_{(1,b)j} = \sum_{strands} (E_t)_{j-1} (\cos \beta_{s,j-1})^3 A_s(D_s(\rho_b)) \int_{L_{j-1}} [N_u]^T [N_u] d\xi \quad (\text{B.4})$$

$$[k]_{(2,b)j} = - \sum_{strands} (E_t)_{j-1} (\cos \beta_{s,j-1})^3 y_{cs} A_s(D_s(\rho_b)) \int_{L_{j-1}} [N_{\theta_z}]^T [N_u] d\xi \quad (\text{B.5})$$

$$[k]_{(3,b)j} = \sum_{strands} (E_t)_{j-1} (\cos \beta_{s,j-1})^3 z_{cs} A_s(D_s(\rho_b)) \int_{L_{j-1}} [N_{\theta_y}]^T [N_u] d\xi \quad (\text{B.6})$$

$$[k]_{(4,b)j} = [[k]_{(2,b)j}]^T \quad (\text{B.7})$$

$$[k]_{(5,b)j} = \sum_{strands} (E_t)_{j-1} (\cos \beta_{s,j-1})^3 \left[ y_{cs}^2 A_s(D_s(\rho_b)) + \frac{I_{ss}(D_s(\rho_b))}{(\cos \beta_{s,j-1})^2} \right] \int_{L_{j-1}} [N_{\theta_z}]^T [N_{\theta_z}] d\xi \quad (\text{B.8})$$

$$[k]_{(6,b)j} = - \sum_{strands} (E_t)_{j-1} (\cos \beta_{s,j-1})^3 y_{cs} z_{cs} A_s(D_s(\rho_b)) \int_{L_{j-1}} [N_{\theta_y}]^T [N_{\theta_z}] d\xi \quad (\text{B.9})$$

$$[k]_{(7,b)j} = [[k]_{(3,b)j}]^T \quad (\text{B.10})$$

$$[k]_{(8,b)j} = [[k]_{(6,b)j}]^T \quad (\text{B.11})$$

$$[k]_{(9,b)j} = \sum_{strands} (E_t)_{j-1} (\cos\beta_{s,j-1})^3 \left[ z_{cs}^2 A_s(D_s(\rho_b)) + \frac{I_{pp}(D_s(\rho_b))}{(\cos\beta_{s,j-1})^2} \right] \int_{L_{j-1}} [N_{\theta_y}]^T [N_{\theta_y}] d\xi \quad (B.12)$$

$$[k]_{(10,b)j} = \sum_{strands} (E_t)_{j-1} (\cos\beta_{s,j-1})^2 \sin\beta_{s,j-1} \sqrt{y_{cs}^2 + z_{cs}^2} A_s(D_s(\rho_b)) \int_{L_{j-1}} [N_{\theta_x}]^T [N_u] d\xi \quad (B.13)$$

$$[k]_{(11,b)j} = - \sum_{strands} (E_t)_{j-1} (\cos\beta_{s,j-1})^2 \sin\beta_{s,j-1} y_{cs} \sqrt{y_{cs}^2 + z_{cs}^2} A_s(D_s(\rho_b)) \int_{L_{j-1}} [N_{\theta_x}]^T [N_{\theta_z}] d\xi \quad (B.14)$$

$$[k]_{(12,b)j} = \sum_{strands} (E_t)_{j-1} (\cos\beta_{s,j-1})^2 \sin\beta_{s,j-1} z_{cs} \sqrt{y_{cs}^2 + z_{cs}^2} A_s(D_s(\rho_b)) \int_{L_{j-1}} [N_{\theta_x}]^T [N_{\theta_y}] d\xi \quad (B.15)$$

$$[k]_{(13,b)j} = \sum_{strands} (E_t)_{j-1} (\sin\beta_{s,j-1})^2 \cos\beta_{s,j-1} (y_{cs}^2 + z_{cs}^2) A_s(D_s(\rho_b)) \int_{L_{j-1}} [N_{\theta_x}]^T [N_{\theta_x}] d\xi \quad (B.16)$$

$$[k]_{(14,b)j} = [[k]_{(10,b)j}]^T \quad (B.17)$$

$$[k]_{(15,b)j} = [[k]_{(11,b)j}]^T \quad (B.18)$$

$$[k]_{(16,b)j} = [[k]_{(12,b)j}]^T \quad (B.19)$$

and

$$[k_G]_{b,j} = \begin{bmatrix} k_{G11} & \cdots & k_{G112} \\ \vdots & \ddots & \vdots \\ k_{G121} & \cdots & k_{G1212} \end{bmatrix}_{b,j} = \sum_{i=1}^{24} [o]_{(i,b)j} \quad (B.20)$$

where

$$[o]_{(1,b)j} = \sum_{strands} (\sigma_{st})_{j-1} (\cos\beta_{s,j-1})^3 A_s(D_s(\rho_b)) \int_{L_{j-1}} [N_u]^T [N_u] d\xi \quad (B.21)$$

$$[o]_{(2,b)j} = - \sum_{strands} (\sigma_{st})_{j-1} (\cos\beta_{s,j-1})^3 y_{cs} A_s(D_s(\rho_b)) \int_{L_{j-1}} [N_{\theta_z}]^T [N_u] d\xi \quad (B.22)$$

$$[o]_{(3,b)j} = \sum_{strands} (\sigma_{st})_{j-1} (\cos\beta_{s,j-1})^3 z_{cs} A_s(D_s(\rho_b)) \int_{L_{j-1}} [N_{\theta_y}]^T [N_u] d\xi \quad (B.23)$$

$$[o]_{(4,b)j} = [[o]_{(2,b)j}]^T \quad (B.24)$$

$$[o]_{(5,b)j} = \sum_{strands} (\sigma_{st})_{j-1} (\cos\beta_{s,j-1})^3 \left[ y_{cs}^2 A_s(D_s(\rho_b)) + \frac{I_{ss}(D_s(\rho_b))}{(\cos\beta_{s,j-1})^2} \right] \int_{L_{j-1}} [N_{\theta_z}]^T [N_{\theta_z}] d\xi \quad (B.25)$$

$$[o]_{(6,b)j} = - \sum_{strands} (\sigma_{st})_{j-1} (\cos\beta_{s,j-1})^3 y_{cs} z_{cs} A_s(D_s(\rho_b)) \int_{L_{j-1}} [N_{\theta_y}]^T [N_{\theta_z}] d\xi \quad (B.26)$$

$$[o]_{(7,b)j} = [[o]_{(3,b)j}]^T \quad (B.27)$$

$$[o]_{(8,b)j} = [[o]_{(6,b)j}]^T \quad (B.28)$$

$$[o]_{(9,b)j} = \sum_{strands} (\sigma_{st})_{j-1} (\cos\beta_{s,j-1})^3 \left[ z_{cs}^2 A_s(D_s(\rho_b)) + \frac{I_{pp}(D_s(\rho_b))}{(\cos\beta_{s,j-1})^2} \right] \int_{L_{j-1}} [N_{\theta_y}]^T [N_{\theta_y}] d\xi \quad (B.29)$$

$$[o]_{(10,b)j} = \sum_{strands} (\sigma_{st})_{j-1} (\cos\beta_{s,j-1})^2 \sin\beta_{s,j-1} \sqrt{y_{cs}^2 + z_{cs}^2} A_s(D_s(\rho_b)) \int_{L_{j-1}} [N_{\theta_x}]^T [N_u] d\xi \quad (B.30)$$

$$[o]_{(11,b)j} = - \sum_{strands} (\sigma_{st})_{j-1} (\cos\beta_{s,j-1})^2 \sin\beta_{s,j-1} y_{cs} \sqrt{y_{cs}^2 + z_{cs}^2} A_s(D_s(\rho_b)) \int_{L_{j-1}} [N_{\theta_x}]^T [N_{\theta_z}] d\xi \quad (B.31)$$

$$[o]_{(12,b)j} = \sum_{strands} (\sigma_{st})_{j-1} (\cos\beta_{s,j-1})^2 \sin\beta_{s,j-1} z_{cs} \sqrt{y_{cs}^2 + z_{cs}^2} A_s(D_s(\rho_b)) \int_{L_{j-1}} [N_{\theta_x}]^T [N_{\theta_y}] d\xi \quad (B.32)$$



$$[o]_{(13,bj)} = \sum_{strands} (\sigma_{st})_{j-1} (\sin\beta_{s,j-1})^2 \cos\beta_{s,j-1} (y_{cs}^2 + z_{cs}^2) A_s(D_s(\rho_b)) \int_{L_{j-1}} [N_{\theta_x}]^T [N_{\theta_x}] d\xi \quad (B.33)$$

$$[o]_{(14,bj)} = [[o]_{(10,bj)}]^T \quad (B.34)$$

$$[o]_{(15,bj)} = [[o]_{(11,bj)}]^T \quad (B.35)$$

$$[o]_{(16,bj)} = [[o]_{(12,bj)}]^T \quad (B.36)$$

$$[o]_{(17,bj)} = \sum_{strands} (\sigma_{st})_{j-1} \cos\beta_{s,j-1} A_s(D_s(\rho_b)) \int_{L_{j-1}} [N_{\theta_z}]^T [N_{\theta_z}] d\xi \quad (B.37)$$

$$[o]_{(18,bj)} = - \sum_{strands} (\sigma_{st})_{j-1} z_{sc} \cos\beta_{s,j-1} A_s(D_s(\rho_b)) \int_{L_{j-1}} [N_{\theta_x}]^T [N_{\theta_z}] d\xi \quad (B.38)$$

$$[o]_{(19,bj)} = [[o]_{(18,bj)}]^T \quad (B.39)$$

$$[o]_{(20,bj)} = \sum_{strands} (\sigma_{st})_{j-1} \cos\beta_{s,j-1} \left[ z_{cs}^2 A_s(D_s(\rho_b)) + \frac{I_{pp}(D_s(\rho_b))}{(\cos\beta_{s,j-1})^2} \right] \int_{L_{j-1}} [N_{\theta_x}]^T [N_{\theta_x}] d\xi \quad (B.40)$$

$$[o]_{(21,bj)} = \sum_{strands} (\sigma_{st})_{j-1} \cos\beta_{s,j-1} A_s(D_s(\rho_b)) \int_{L_{j-1}} [N_{\theta_y}]^T [N_{\theta_y}] d\xi \quad (B.41)$$

$$[o]_{(22,bj)} = \sum_{strands} (\sigma_{st})_{j-1} y_{sc} \cos\beta_{s,j-1} A_s(D_s(\rho_b)) \int_{L_{j-1}} [N_{\theta_x}]^T [N_{\theta_y}] d\xi \quad (B.42)$$

$$[o]_{(23,bj)} = [[o]_{(22,bj)}]^T \quad (B.43)$$

$$[o]_{(24,bj)} = \sum_{strands} (\sigma_{st})_{j-1} \cos\beta_{s,j-1} \left[ y_{cs}^2 A_s(D_s(\rho_b)) + \frac{I_{ss}(D_s(\rho_b))}{(\cos\beta_{s,j-1})^2} \right] \int_{L_{j-1}} [N_{\theta_x}]^T [N_{\theta_x}] d\xi \quad (B.44)$$

in which  $(z_{cs}, y_{cs})$  are the coordinates of the centroid of the strand  $s$  relative to the centroid of the rope cross-section;  $A_s$  is the cross-sectional area of the strand  $s$ ;  $I_{ss}$  and  $I_{pp}$  are the moments of inertia of each strand relative to its local reference system; and  $\sigma_{st}$  is the normal stress of the strand  $s$  along its local longitudinal axis  $t$ ; and  $L_{j-1}$  is the updated length of the cable-beam element  $b$  at the end of the  $(j-1)$  step of the analysis.

### Appendix C. Global stiffness matrices and nodal load vectors

$$[k_g]_{bb,j-1}^{k-1} = [\Gamma]_{bb,j-1}^{T,k-1} [k]_{bb,j-1}^{k-1} [\Gamma]_{bb,j-1}^{k-1} \quad (C.1)$$

$$\{P_g\}_{bb,j}^k = [\Gamma]_{bb,j}^{T,k} \{P\}_{bb,j}^k \quad (C.2)$$

$$\{Q_g\}_{bb,j}^k = [\Gamma]_{bb,j}^{T,k} \{Q\}_{bb,j}^k \quad (C.3)$$

in which the subscript  $g$  refers to global coordinates. The transformation matrices  $[\Gamma]_b$  account for the direction cosines between the local and global coordinate systems as discussed in [33,39] among others.

### Appendix D. Increment values of unbalanced line forces

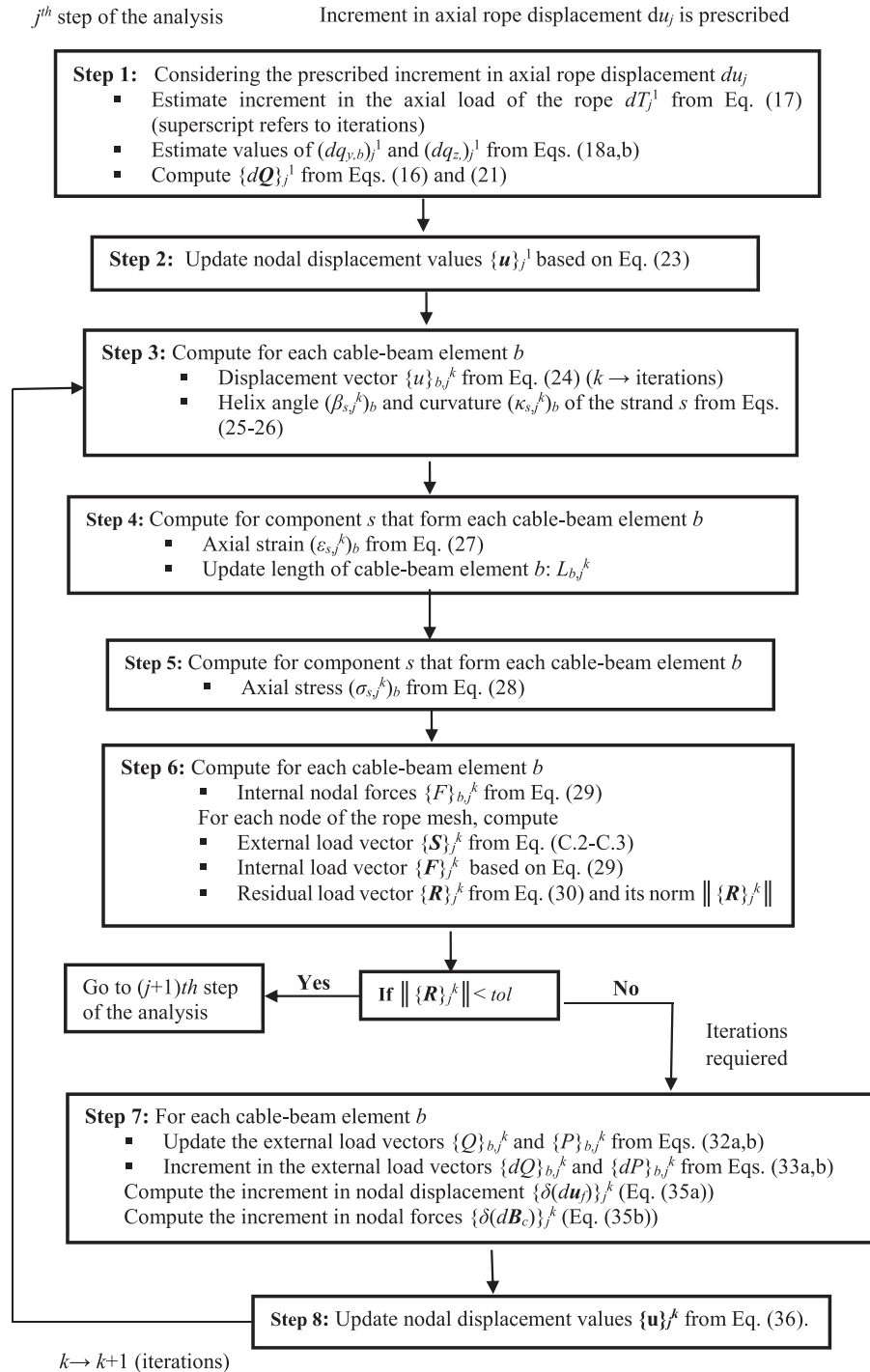
The constants  $G_i$  ( $i = 1, 2$ ) in Eqs. (18a,b) have the following expressions:

$$G_1 = 1 - 2(1 - D_s(\rho_b)) \sin\psi_s \quad (D.1)$$

$$G_2 = 2 \sin\psi_s - (1 - D_s(\rho_b)) \quad (D.2)$$

where  $D_s(\rho_b)$  is the damage index of each strand that forms a cable-beam element  $b$  given by Eq. (B.2); and  $\psi_s$  is the angle between the contact line force direction of strand which points to the centroid of the equilateral triangle that forms the three-strand configuration.

Appendix E. Flow chart of the NLCBM numerical algorithm



References

[1] Chaplin CR. Torsional failure of wire rope mooring line during installation in deep water. *Eng Fail Anal* 1998;6:67–82.  
 [2] Utting WS, Jones N. A survey of literature on the behaviour of wire ropes. *Wire Ind* 1984;51:623–9.  
 [3] Foster GP. Advantages of fiber rope over wire rope. *J Ind Text* 2002;32:67–75.  
 [4] McKenna HA, Hearle JSW, O'Hear N. *Handbook of Fibre Rope Technology* Cambridge, England; 2004.  
 [5] Chaplin CR. The fatigue and degradation mechanisms of hoisting ropes. In: Hoist

and Haul Conference 2005, Perth, Australia, 359–66.  
 [6] Mouradi H, El Barkany A, El Biyaali A. Investigation on the main degradation mechanisms of steel wire ropes. *J Eng Applied Sci* 2016;100:1206–17.  
 [7] Cholewa W. Wire fracture and weakening of wire rope. In: *Wire rope discard criteria: round table conference*. Swiss Federal Institute of Technology (ETH), Institute of Lightweight Structures and Ropeways, September, Zurich, Switzerland; 1989.  
 [8] Evans JJ, Ridge IML, Chaplin CR. Wire failures in ropes and their influence on local wire strain behavior in tension–tension fatigue. *J Strain Anal* 2001;36:231–44.  
 [9] Li D, Miyase A, Williams JG, Wang SS. Damage tolerance of synthetic-fiber mooring ropes: small-scale experiments and analytical evaluation of damaged subropes and

- elements. Technical report, CEAC-TR-03-0101, University of Houston; 2002.
- [10] Ward EG, Ayres R, Banfield S, O'Hear N. Full scale experiments on damaged polyester rope. Technical report, JIP-FP-1. Offshore Technology Research Center 2006.
- [11] Liu X, Lian Y, Li L, Zhang Y. Experimental investigation on dynamic stiffness of damaged synthetic fiber ropes for deepwater moorings. *J. Offshore Mech Arct* 2015;137: 061401–1–8.
- [12] Mouradi H, El Barkany A, El Biyaali A. Steel wire ropes failure analysis: Experimental study. *Eng Fail Anal* 2018;91:234–42.
- [13] Beltran JF, Nuñez E, Nuñez F, Silva I, Bravo T, Moffat R. Static response of asymmetrically damaged metallic strands: Experimental and numerical approach. *Constr Build Mater* 2018;192:538–54.
- [14] Lanteigne J. Theoretical estimation of the response of helically armoured cables of tension, torsion, and bending. *J Appl Mech* 1985;52:423–32.
- [15] MacDougall C, Bartlett F. Mechanical model for unbonded seven-wire tendon with symmetric wire breaks. *J Eng Mech* 2005;131:1239–47.
- [16] MacDougall C, Bartlett F. Mechanical model for unbonded seven-wire tendon with single broken wire. *J Eng Mech* 2006;132:1345–53.
- [17] Lepidi V, Gattulli V, Vestroni F. Static and dynamic response of elastic suspended cables with damage. *Int. J. Solids Struct* 2007;44:8194–212.
- [18] Meksem A, El Ghorba M, Benali A, El Barkany A. Optimization by the reliability of the damage by tiredness of a wire rope of lifting. *Appl Mech Mater* 2011;61:15–24.
- [19] Beltran JF, Williamson EB. Numerical procedure for the analysis of polyester damaged ropes. *Eng Struct* 2011;33:1698–709.
- [20] Beltran JF, Vargas D. Effect of broken rope components distribution throughout rope cross-section on polyester rope response: Numerical approach. *Int J Mech Sci* 2012;64:32–46.
- [21] Beltran JF, De Vico E. Assessment of static rope behavior with asymmetric damage distribution. *Eng Struct* 2015;86:84–98.
- [22] Fontanari V, Benedetti M, Monelli B. Elasto-plastic behavior of a Warrington-Seale rope: Experimental analysis and finite element modeling. *Eng Struct* 2015;82:113–20.
- [23] Beltran JF, Ramirez N, Williamson EB. Simplified analysis of the influence of strain localization and asymmetric damage distribution on static damaged polyester rope behavior. *Ocean Eng* 2017;145:237–49.
- [24] Lacarbonara W. *Nonlinear Structural Mechanics: Theory, dynamical phenomena and modeling*. NY, USA: Springer-Verlag; 2013.
- [25] Luongo A, Zulli D. *Mathematical models of beams and cables*. NJ, USA: Wiley & Sons Inc; 2013.
- [26] Power Guérard S. *line conductors, a contribution to the analysis of their dynamic behaviour* PhD thesis Belgium: Université de Liège; 2011.
- [27] Fang ZF, He QS, Xiang BF, Xiao HP, He KD, Du YX. A finite element cable model and its applications based on the cubic spline curve. *China Ocean Eng* 2013;27:683–92.
- [28] Quan WC, Zhang ZY, Zhang AQ, Zhang QF, Tian Y. A geometrically exact formulation for three-dimensional numerical simulation of the umbilical cable in a deep-sea rov system. *China Ocean Eng* 2015;29:223–40.
- [29] Foti F, Martinelli L. Mechanical modeling of metallic strands subjected to tension, torsion and bending. *Int J Solids Struct* 2016;91:1–17.
- [30] Lalonde S, Guilbault R, Légeron F. Modeling multilayered wire strands, a strategy based on 3D finite element beam-to-beam contacts - Part I: Model formulation and validation. *Int J Mech Sci* 2017;126:281–96.
- [31] Eidvisk O, Schjølberg I. Finite element cable-model for remotely operated vehicles (ROVs) by application of beam theory. *Ocean Eng.* 2018;163:322–36.
- [32] Ruiz R, Loyola L, Beltran JF. Numerical framework for stress cycle assessment of cables under vortex shedding excitations. *Wind Struct* 2019;28:225–38.
- [33] Yang YB, Kuo SR. *Theory and analysis of nonlinear framed structures*. first ed. Singapore: Prentice Hall; 1994.
- [34] Hartmann F, Katz C. *Structural analysis with finite elements*. second ed. Berlin: Springer-Verlag; 2007.
- [35] Reddy JN. *An introduction to nonlinear finite element analysis*. second ed. Oxford: Oxford University Press; 2015.
- [36] Raoof M. Wire recovery length in a helical strand under axial fatigue loading. *Int J Fatigue* 1991;13:127–32.
- [37] Beltran JF, Williamson EB. Numerical simulation of damage localization in polyester mooring ropes. *J Eng Mech* 2010;136:945–59.
- [38] Costello GA. *Theory of wire rope*. first ed. New York: Springer-Verlag; 1990.
- [39] Bathe KJ. *Finite element procedures*. New Jersey: Prentice-Hall; 1996.
- [40] Leech CM. *Aspects of modeling of synthetic fibre rope*. Proceedings of Marine Technology Society Conference, Washington, DC; 1990.
- [41] Bravo T. *Estimación numérica de la respuesta estática de un cable dañado: Formulación viga-cable*. MSc thesis. Chile: University of Chile; 2018.
- [42] Lemaitre J, Chaboche J. *Mechanics of Solids Materials*. Cambridge: Cambridge University Press; 1990.